EXPERIMENTAL STUDY OF TURBULENCE PAST THIN TABS

BY

AXY PAGAN-VAZQUEZ

THESIS

Submitted in partial fulfillment of the requirements
for the degree of Master of Science in Mechanical Engineering
in the Graduate College of the
University of Illinois at Urbana-Champaign, 2016

Urbana, Illinois

Adviser:

Assistant Professor Leonardo P. Chamorro

Abstract

The turbulence past thin tabs of rectangular, triangular, and ellipsoidal geometries is experimentally investigated using particle image velocimetry at Reynolds number Re=2000 and Re=12900 based on the tabs height and freestream velocity. Turbulence statistics including streamwise velocity, turbulent kinetic energy (TKE), and vortex swirling strength are obtained in the symmetry plane of each tab. The results show a strong dependency of the tab geometry on the strength of the induced vortical structures at the low Re. The turbulent flow regime at high Re promotes high shear stress and TKE production right past the tabs, where the rectangular tab induces greater mixing. The spanwise vortices from the rectangular tab have an average vortex cores radius 20% larger and nearly 30% greater circulation as compared to those from the ellipsoidal tab. Compared to the ones produced by the triangular tab, the core radius is 25% larger and the circulation is almost 50% higher. Our results also show, for the first time, that hairpin structures are possible in triangular tabs. Finally, we conclude that geometrical singularity plays an important role in the strength of the primary vortical structures shed by the tabs.

To Marian

Acknowledgments

I would like to thank Prof. Leonardo P. Chamorro to trace and guide the academic path. I would like to extend my gratitude Dr. Charlie Marsh for his wisdom and the opportunity to pursue a M.S. degree while holding high responsibilities as part of the professional staff at the Construction Engineering Research Laboratory. My heartfelt gratitude to all the faculty and students involved in this research, especially to the Ph.D. candidate, Mr. Ali Hamed for all his help and patience running experiments. Finally, I would like to thank my family, especially my partner Marian, who has given me tremendous support throughout all these years of continuous dedication and work.

Table of Contents

List of Abbreviations

CCD	Charge-Coupled Device
CVP	Counter-Rotating Vortex Pair
DNS	Direct Numerical Simulation
FOV	Field of View
K-H	Kelvin-Helmholtz instability
LES	Large Eddy Simulation
N-S	Navier-Stokes
PIV	Particle Image Velocimetry
RIM	Refractive Index Matching
TKE	Turbulent Kinetic Energy
VG	Vortex Generator

List of Symbols

h_T	vortex generator tab height
E_{TK}	Turbulent Kinetic Energy Production
Re	Reynolds Number
w	vortex generator tab base width
r_c	vortex core radius
r_{cr}	averaged core radii of the vortices induced by the rectangular tab
U_0	bulk velocity
U	streamwise mean velocity
V	wall-normal mean velocity
u'	streamwise velocity fluctuation
u''	LES-like decomposed velocity field
$\widetilde{u}$	filtered velocity
v'	wall-normal velocity fluctuation
x	spanwise coordinate
y	wall-normal coordinate
δ_{99}	boundary layer thickness
λ_{ci}	vortex swirling strength
ν	kinematic viscosity
ρ	fluid density
θ	inclination angle of the tabs
Γ	circulation
Γ_r	averaged circulation of the hairpin vortices (head) induced by the rectangular tab
Λ_{ci}	signed of λ_{ci}
∇	gradient operator

Chapter 1

Background

Characterization of Bluff body-induced flow perturbations has been a problem of high interest since the last century among scientists and engineers due to its common but complex varied occurrence. Aerodynamists carefully consider its impacts on the drag, flow separation, and turbulent wake. Bluff bodies are also widely used to trigger and enhance turbulence in laminar or low turbulent flow regimes [1]. These could include industrial chemical processes, where reaction efficiency strictly relies on solution homogeneity, particulate distribution, among others [2]. Similarly, compact bodies known as vortex generators (VGs) have been used to enhance the heat transport in a flow. Their applications range from Stokes microfluidics mixing [3, 4], heat sink cooling capacity increase [5], ultrasonic heat measurement accuracy enhancement [6], and heat exchanger and overall transfer efficiency improvement [7–9].

The mixing effects produced by VGs have been extensively studied experimentally [10–12] and numerically [13–15]. Many of these studies have focused on understanding the interactions of vortical flow structures and their impact in the surrounding flow field. Parametric studies, including VG shape, relative location, and Re conditions were pioneered by Gretta [16]. He speculated about the formation of a shear layer and vortices that separate the high and low flow regimes. Also, he quantified the fluid injection and ejection distance that penetrate the shear layer, providing a better understanding of the flow around VGs. The trapezoidal-shaped VG tabs keep the optimum balance between downstream flow mixing and reduced pressure decay. Further studies discuss the development of the predominant vortex structures such as the Counter Rotating Vortex Pair (CVP) [17], [18]. This structure, has shown to produce significant mixing in the wake of the tab. It acts as artificial mechanical agitators in the surrounding field [19]. Although these well-defined vortex structures remarkably entrail the fluid from the high to low and low to high flow regions, the CVP effective mixing action is considerably limited to short downstream distances.

Hairpin-like vortices with the head predominantly rotating in the spanwise direction have been found to impulse the fluid transport between the mean flow and VG wake [20]. The hairpin vortices are developed from the rolling-up process caused by the Kelvin-Helmholtz (K-H) in the shear layer, extending down as "legs" to the bottom wall. Yang [21] emphasized that both, the CVP and the hairpin vortices contribute to the net low velocity fluid ejection from the bottom surface to the shear layer. The two kinds of vortex structure development mechanisms, stability, and longevity can be significantly different. Elavarasan [22] pointed that the CVP, formed in a roll-up process as the result of the existing pressure differences between the VG top and bottom, prevails as the main mixing mechanism limited to ∼1.5 times the VG height. In contrast, hairpin vortices might last up to ∼10 times the VG tab height before they start to lose strength and structure. Consequently, the hairpin vortices might perpetrate higher mixing and homogeneity than the CVP far downstream.

The flow past a trapezoidal tab, including very detailed aspects about vortex formation mechanisms and development, was comprehensively evaluated by Dong and Meng [23] using Direct Numerical Simulation (DNS). They confirmed that CVP and hairpin vortices form at different VG tab locations and that their highest mixing influence situates at distinct spatial regions. Accordingly, the pressure differential between top and bottom tab surface induces a twisting motion, mostly generated from the tab side edges, sparking the CVP structures. Further evaluation could lead to understand what particular VG features have the highest influence over the strong shear layer interaction leading to hairpin vortices development. Still, the K-H instability and hairpin structures formation allude to the VG tab edge contour relationship toward the near and far field effects.

Despite the various studies addressing VG effects on vortex strength and development, to the best of the authors knowledge, none of them have experimentally investigated the role of geometrical singularity on vortex development. The work presented here experimentally addresses this problem by evaluating three vortex generators having two (rectangular), one (triangular), and zero (semi-ellipse) geometrical singularities. These shapes were characterized in a refractive-index-matching environment in combination with the High-Resolution particle image velocimetry (PIV) technique at two Reynolds numbers spanning one order of magnitude. The experimental setup is described in chapter 2, the results are analyzed and discussed in chapter 3, and the conclusions are given in chapter 4.

Chapter 2

Experimental Methods

Rectangular, triangular, and ellipsoidal tab geometries were studied in a 2.5 m long refractive index matching (RIM) channel with a squared cross section of 112.5 mm × 112.5 mm. All tabs were machined from smooth acrylic plates with 1.6 mm thickness. The tabs were inclined at an angle $\theta = 24.5^o$ and had a base of $w = 28.3$ mm and a height $h_T = 17$ mm. The tab geometries, shown in figure. 2.1 and figures B.1-B.3, were chosen in accordance with previous work [20, 23, 24] to facilitate comparisons when appropriate. The refractive index of the working fluid (63% by weight of a sodium iodide solution) was matched to that of the tabs through careful temperature control. The solution has a density $\rho \simeq 1800$ kg m^{-3} and a kinematic viscosity $\nu \simeq 1.1 \times 10^{-6}$ m^2 s^{-1}. More details on the RIM channel can be found in Hamed *et al.* [25] and Blois *et al.* [26]. Refractive index matching renders the tabs invisible granting unobstructed optical access, minimizing aberrations, and allowing for measurements to be made very close to tab surface.

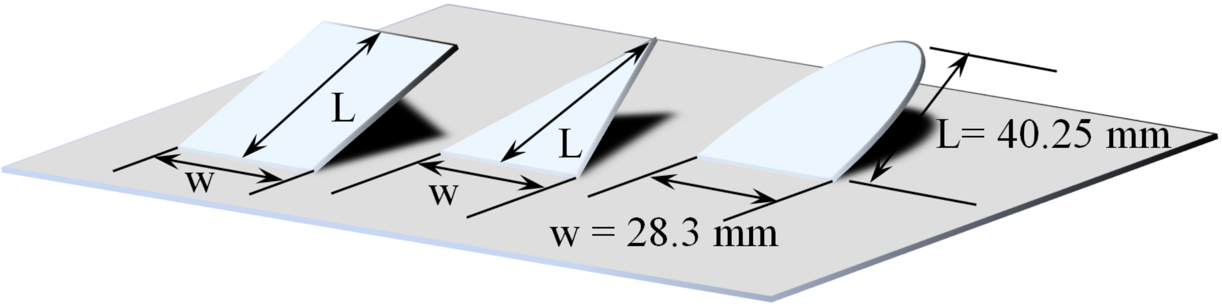

Figure 2.1: Vortex generator tab geometries used in this work.

The tabs were placed on the back wall of the RIM channel approximately $90h_T$ from the inlet (see Fig. 2.2 for experimental setup). The flow around each tab was studied at Re based on tab height and incoming freestream velocity 2000 (low Re) and 12900 (high Re). The boundary layer thickness δ_{99} at a distance $3h_T$ preceding the tab is $\delta_{99}/h_T \sim 1$ and $\delta_{99}/h_T \sim 1.5$ for the low and high Re, respectively. Two-dimensional PIV measurements were made in a streamwise-oriented wall-normal plane coinciding with the center of both, the tab and the channel. The working fluid was seeded with 14 μm silver-coated hollow glass spheres. A field of view (FOV) 190.2 mm × 126.8 mm was illuminated using a 1 mm thick laser sheet supplied by a 250 mJ/pulse double-pulsed laser from Quantel. Four thousand image pairs for each case (three tabs, two Re) were captured at a frequency of 1 Hz by an 11 MP, 12 bit, frame-straddle, CCD camera. Figures 2.2 and

2.3 show the experimental setup schematics, including FOV details and the RIM flume setup, respectively. Image pairs were interrogated with a recursive cross-correlation method using Insight 4G software package from TSI. The final interrogation window is 16 × 16 pixels with 50% overlap resulting in a final vector grid spacing $\Delta x = \Delta y = 382$ μm.

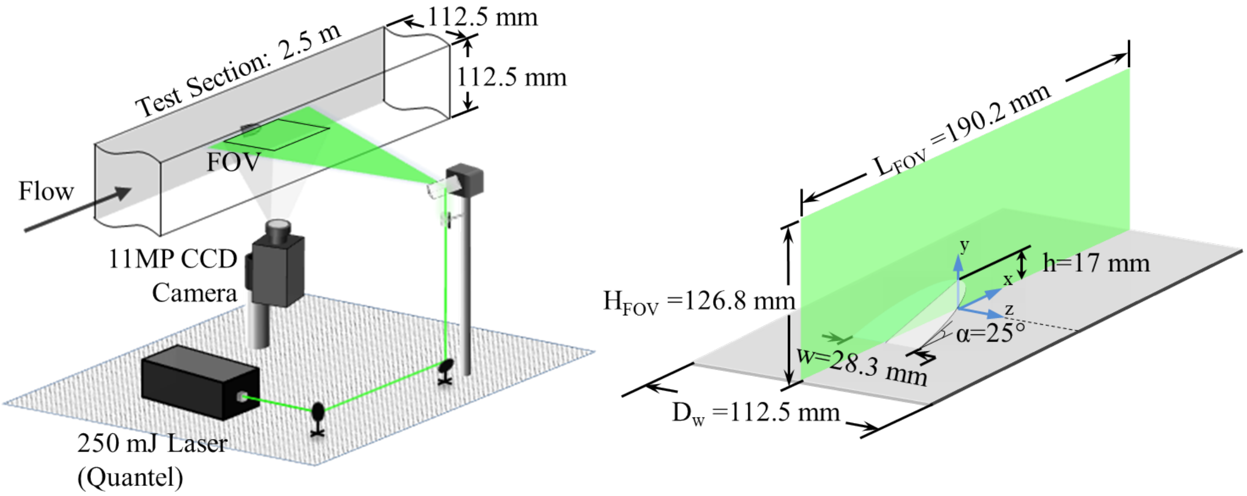

Figure 2.2: Schematics of the experimental setup and details of the field of view.

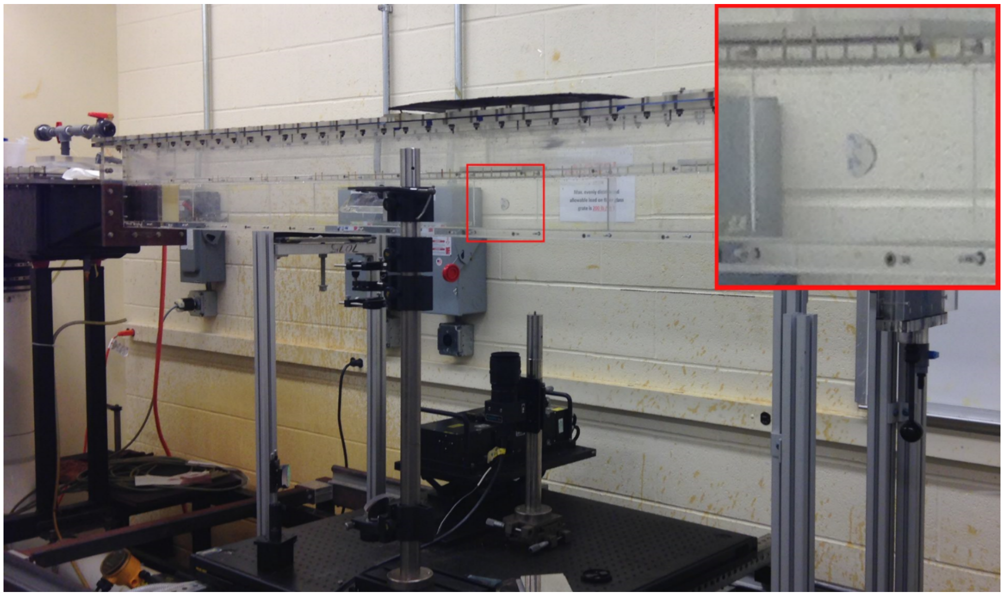

Figure 2.3: Refractive Index Matching (RIM) flume with basic setup. The ellipsoidal tab is highlighted in the red square.

Chapter 3

Results and Discussion

The experiments are designed to investigate the effect of the sharp edges in planar VGs on the induced turbulence and large-scale vortex structures at two Re numbers spaced one order of magnitude. The tabs under study have two (rectangular), one (triangular), and zero (elliptical) corners, and they share the same base w, and height h_T. The normalized streamwise (U/U_o) and vertical (V/U_o) velocity components, turbulent kinetic energy $TKE = \langle u'u' + v'v' \rangle / 2U_0^2$, kinematic shear stress $-\langle u'v' \rangle / U_0^2$, turbulent kinetic energy production $E_{tk} h_T / U_0^3$, and instantaneous fields of swirling strength $\Lambda_{ci} h_T / U_0$ are obtained in a vertical plane coincident with the axis of the tabs between $x/h_T \in [-3, 6]$ and $y/h_T \in [0, 4]$. The base of the tabs is located at $x/h_T = -2$, the operator $\langle\ \rangle$ indicates time averaging, and u' and v' are the fluctuating components of the streamwise and vertical velocity, respectively.

3.1 Streamwise Velocity Distribution

Distinctive footprint of the tabs on the flow for the two Re is already evident from the first order statistics. Figure 3.1 shows selected vertical profiles of U/U_o for the 3 tabs at x/h_T =-3, -2, -1, 0, 1, 2, 3, 4, and 5. The profiles do not exhibit differences upstream and right on the tabs, suggesting that the flow condition among the various cases was the same, which ensures a fair comparison. The mean flow downstream of the triangular and elliptical tabs exhibits practically the same sharp shear layer developed at the tip; however, the shear layer from the rectangular tab is systematically located above the other geometries in the two Re cases. This shear layer characteristic implies higher momentum deficit in the wake of the rectangular VG, possibly due to the larger span of this tab at the top surface. The same argument can be used to explain the lowest momentum deficit near the wall in the wake of the triangular tab. Enhanced mixing promoted by higher turbulence in the large Re induces more similar velocity profiles across the tabs. The apparent Re dependence occurs due to the different flow regimes, laminar vs. turbulent, modulating the dynamics in the wake of the tabs. A local region of negative velocity at the upstream side of the base of the tabs indicates the existence of a recirculating bubble only in the low Re case. There is also a backward flow concentrated at the downstream side of the tabs base at the two Re; however, it extends up to $x/h_T \sim 3$ only in the wake of the rectangular tab at the low Re.

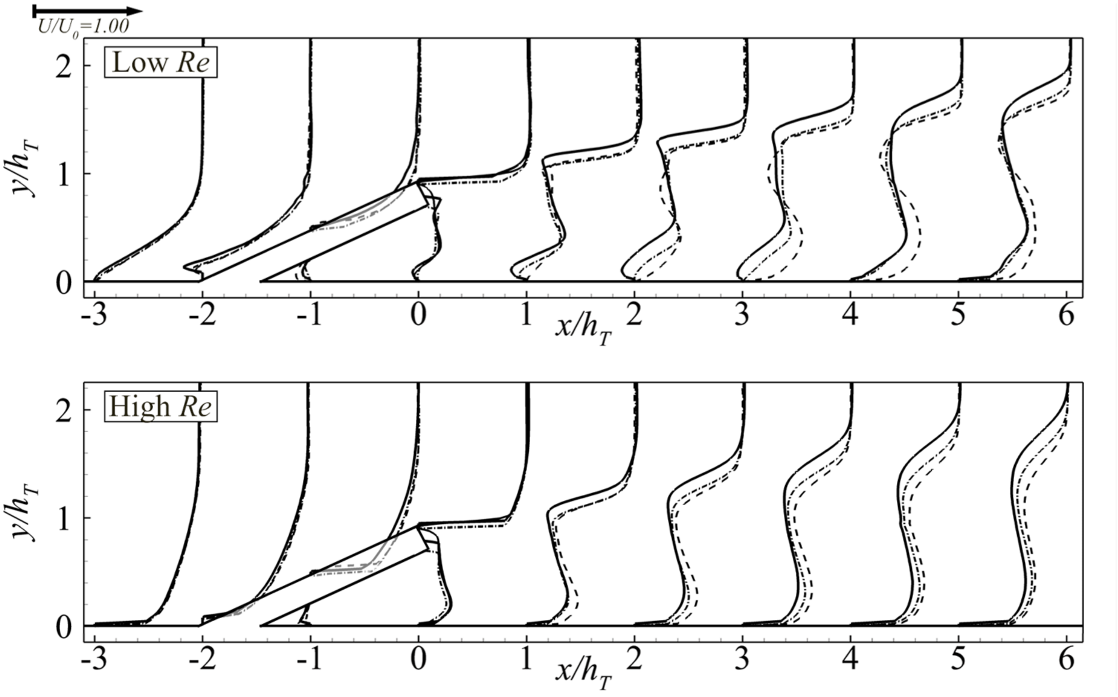

Figure 3.1: Time-averaged normalized streamwise velocity profiles U/U_0 at x/h_T =-3, -2, -1, 0, 1, 2, 3, 4 and, 5 for low Re =2000 and high Re=12900. Rectangular, triangular, and ellipsoidal geometries represented by solid, dashed, and dash-dotted lines, respectively.

3.2 Wall-normal Velocity Distribution

The normalized, time-averaged wall-normal velocity contours V/U_0, given in figure 3.2, show a region downstream of the tab exhibiting high upward flow exceeding 30% U_0. This enhanced vertical flow is associated with the interaction of the counter rotating vortex pair discussed earlier, resulting in the upward entrainment of fluid at the central plane of the tab. Dong, among others [23], have shown that the *K-H* instability, discussed in the context of figure 3.2, interferes with the counter rotating vortex pair, affecting its coherence and ability to entrain fluid upwards. As we show later herein, this instability forms further upstream for the high *Re* case leading to the interruption of the high vertical flow region seen in figure 3.2. For the low *Re*, a recirculation bubble forms upstream at the base of the tabs and acts as further flow blockage. The lack of this recirculation zone at the high *Re* manifests in a higher vertical velocity upstream of the tab. In addition to *Re* effects, the tab geometry plays a significant role by governing the wall-normal flow distribution. This flow distribution is highlighted by the iso-velocity dashed line in figure 3.2, which encompasses the region where $V \geq 5\%\ U_0$. Comparing across the three geometries, the rectangular tab draws the largest amount of fluid up to the channel center. This is explained by the larger surface area facing the flow, leading by continuity to a decrease in streamwise velocity and increase in wall-normal and lateral flows. Among the three geometries, the rectangular tab shows to be more efficient in enhancing vertical transport.

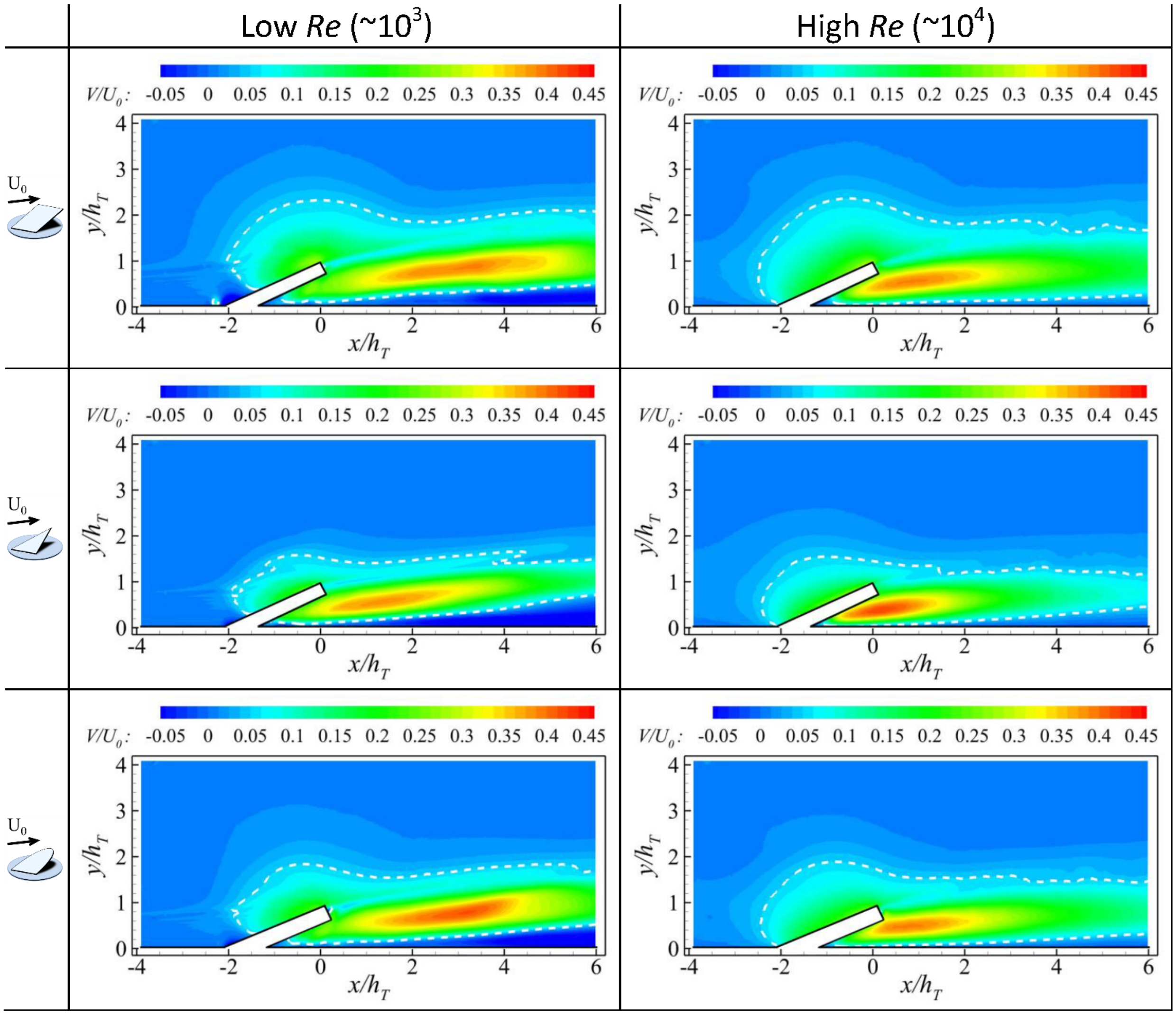

Figure 3.2: Normalized wall-normal velocity component contour V/U_0 at low Re =2000 and high Re=12900. All the figures share the same color levels to aid comparison. White, dashed lines indicate the velocity levels where $V = 0.05U_0$

3.3 Turbulent Kinetic Energy Distribution and Reynolds Stress

The turbulent kinetic energy (TKE) fields reveal substantial differences in the flow downstream of the tabs with respect to the Reynolds number. Specifically, the turbulence levels are noticeable only after $x/h_T \sim 2-3$ in the low Re case. This turbulence distribution suggests that right downstream the tabs, the flow is essentially laminar and instabilities should appear on the high shear layer region where the wake and the external flow interact (figure 3.3). The flow instability results in turbulence and triggers the comparatively high TKE located around the mentioned shear layer. In contrast, the flow experiences transition to turbulence right past the tabs in the high Re, which is evidenced from the TKE levels across the wake with local maximum on the shear layer.

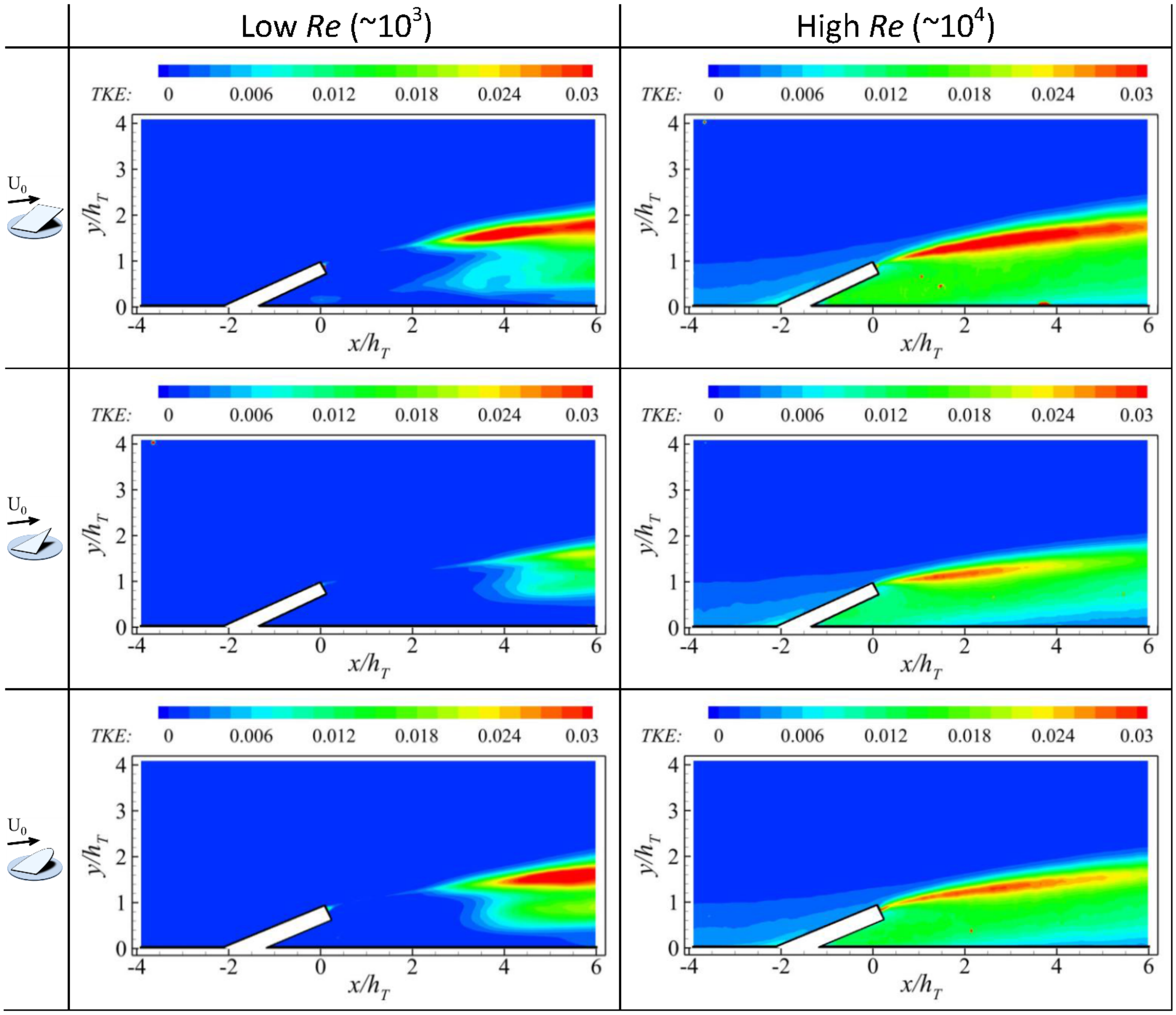

Figure 3.3: 2D contours of TKE around the rectangular, triangular, and elliptical tabs at low Re =2000 and high Re=12900. All the figures share the same color levels to aid comparison.

Differences between the velocity fluctuations induced by each tab are stressed on the 1D profiles illustrated in figure 3.4, which include the same locations given in figure 3.4. Surprisingly, the highest *TKE* levels occur with the ellipsoidal tab (at $x/h_T = 5$), and rectangular tabs for the low and high *Re*; whereas at the other end, the wake from the triangular tab exhibits the lowest *TKE* across *Re*. The 1D *TKE* profiles also highlight a secondary region, very different for each tab, of relatively high *TKE* below the shear layer at the low *Re*. This region is not clear from the ligh *Re*, probably due to the comparatively stronger mixing promoted by broader spectrum of turbulent scales.

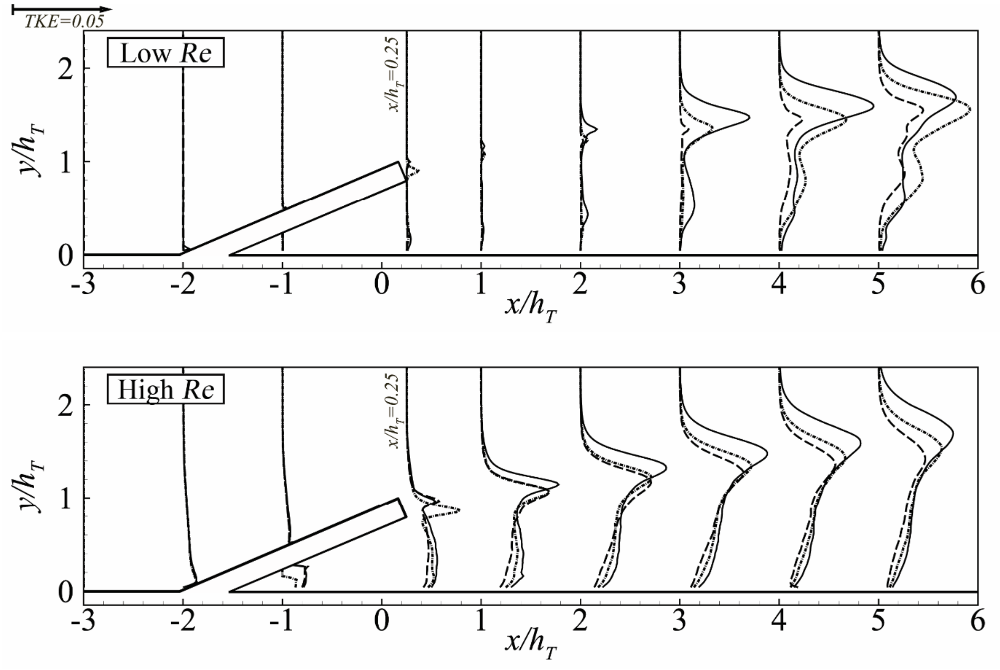

Figure 3.4: 1D TKE ($= \langle u'u' + v'v' \rangle / 2U_0^2$) profiles around the rectangular, triangular, and elliptical tabs at x/h_T =-3, -2, -1, 0.25, 1, 2, 3, 4, and 5 for low Re =2000 and high Re=12900. Rectangular, triangular and ellipsoidal geometries represented by solid, dashed, and dash-dotted lines, respectively.

Analogous to *TKE*, the normalized Reynold Shear Stress $-\langle u'v' \rangle / U_0^2$ (figure 3.5) exhibits non-negligible shear interactions at distances over two tab heights in the low *Re*. However, this occurs right past the tab for the high *Re*. The rectangular geometry manifests greater $-\langle u'v' \rangle$. A notable distinction from *TKE* is the negative shear stress depicted below the shear layer interface, especially at the low wall-normal region. This behavior can be related to the flow profiles shown in figure 3.1, where the transition between strong positive and negative stresses highlights the local streamwise velocity maxima and minima of the tab wake region.

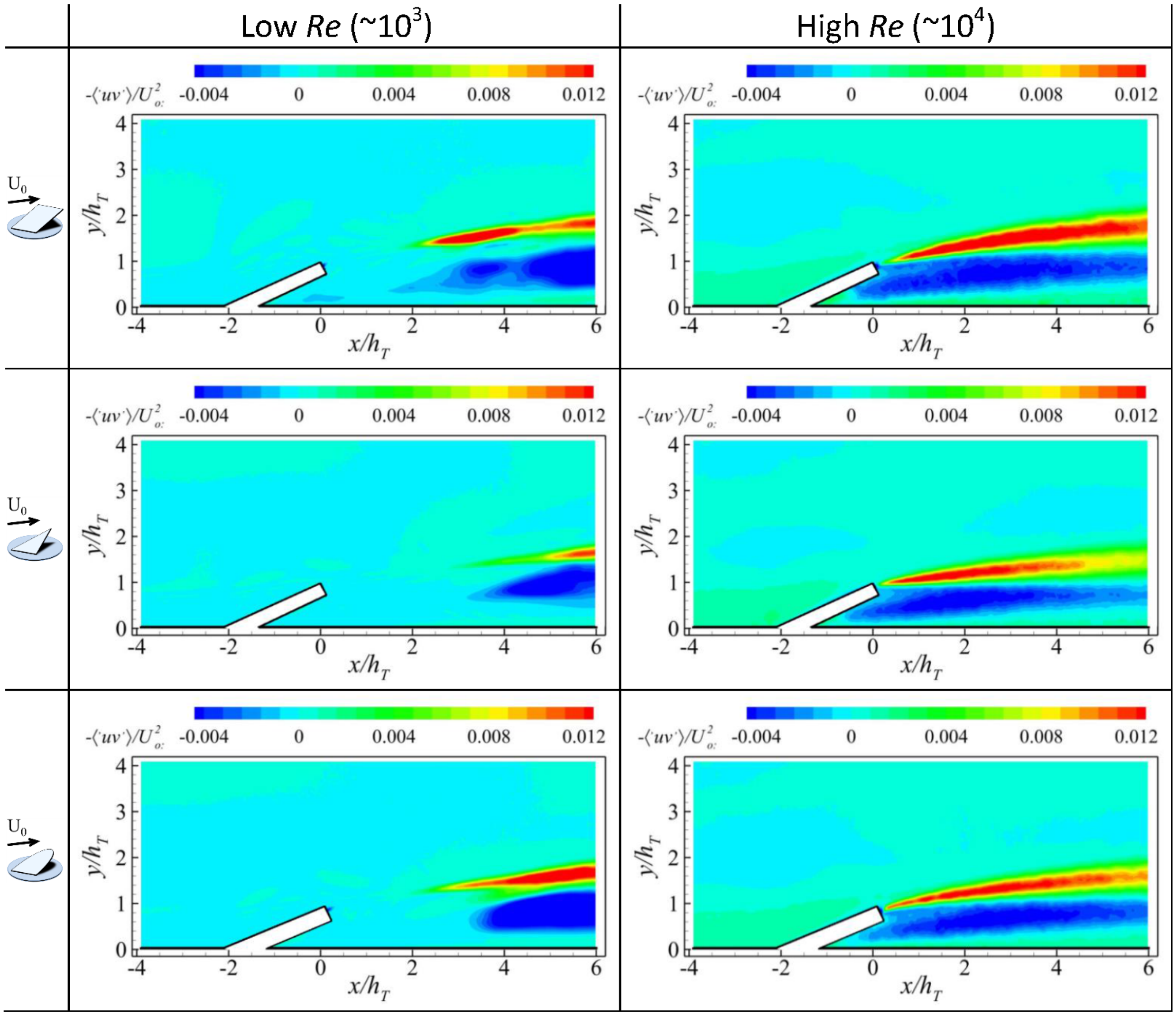

Figure 3.5: 2D contours of $-\langle u'v'\rangle/U_0^2$ around the rectangular, triangular, and elliptical tabs at low Re =2000 and high Re=12900. All the figures share the same color levels to aid comparison.

3.4 Turbulence Energy Production

The turbulent kinetic energy production E_{tk} normalized by h_T/U_0^3 is directly obtained from the *TKE* budget, as indicated in equation 3.1:

$$E_{tk} = -\langle u'v'\rangle\frac{\partial U}{\partial y} - \langle u'^2\rangle\frac{\partial U}{\partial x} - \langle u'v'\rangle\frac{\partial V}{\partial x} - \langle v'^2\rangle\frac{\partial V}{\partial y} \qquad (3.1)$$

The corresponding E_{tk} spatial distribution for all the tabs at the two Re is illustrated in figure 3.6. Similar to the *TKE*, the highest E_{tk} levels occur within the shear layer. It is also noticed that at higher Re the *TKE* is produced right past the tabs, while at $\sim x/h_T \geq 2$ in the low Re. Similarly, a sink of

TKE occurs right downstream of the tabs and near the surface for the high *Re* case and within the wake at similar locations in the low *Re*. Overall, the E_{tk} distribution shows distinctive differences only in the low *Re*, suggesting that the effects of the tab geometry are more dominant within low *Re*.

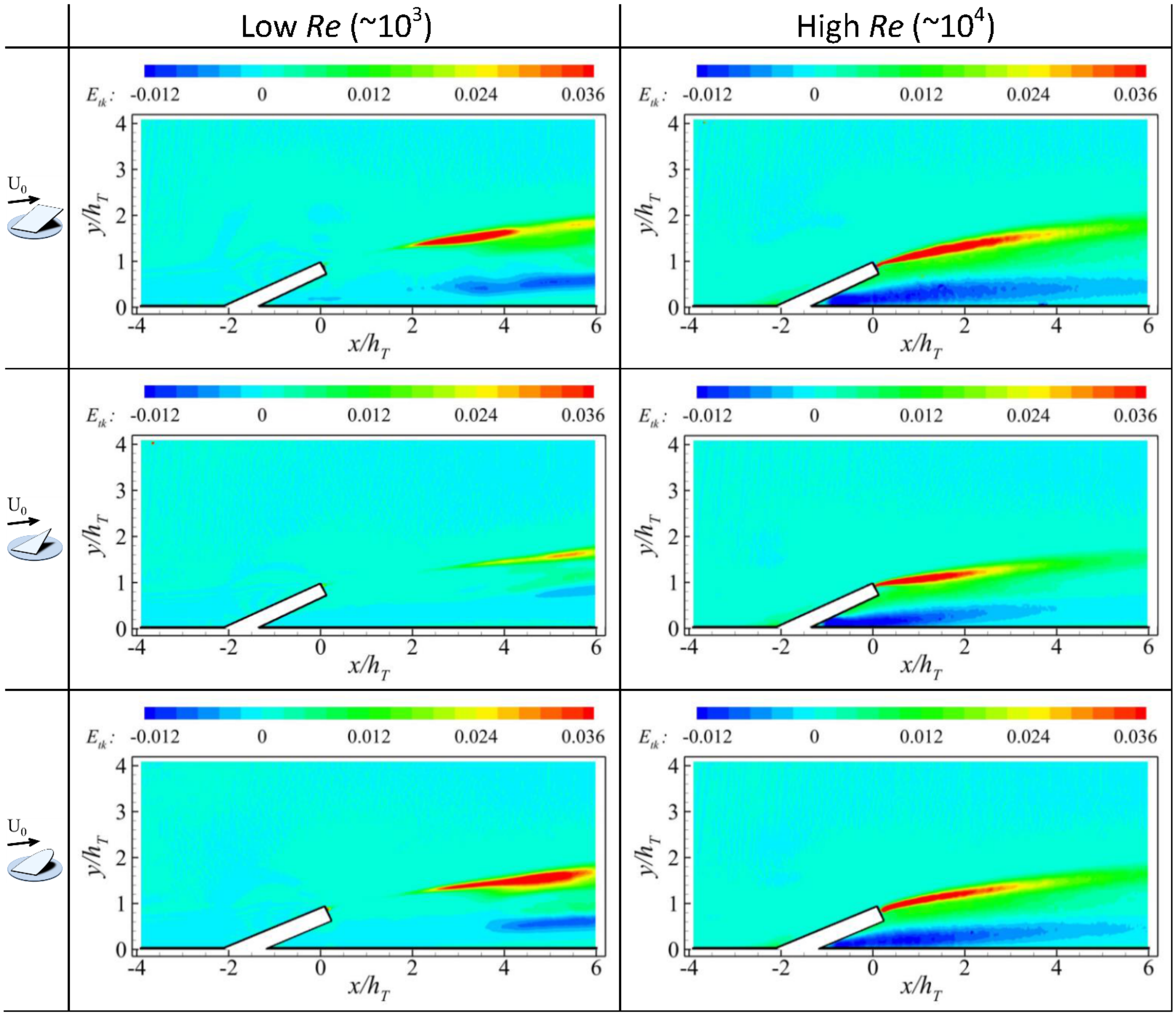

Figure 3.6: 2D contours of $E_{tk}h_T/U_0^3$ around the rectangular, triangular, and elliptical tabs at low *Re* =2000 and high *Re*=12900. All the figures share the same color levels to aid comparison.

3.5 Tab-induced Vortex Strength

Representative instantaneous signed swirling strength Λ_{ci} obtained from the velocity fields is computed to identify primary and dominant vortex structures in all the tab geometry cases and the two *Re* are shown in figure 3.7. The λ_{ci} is the complex conjugate imaginary eigenvalue of the velocity gradient tensor, which defines the vortex swirling strength (Zhou *etal.* [27]). Following Hamed *et al.* [28], an LES-like decomposition is applied to the instantaneous velocity field and superimposed to the Λ_{ci} field to better uncover the vortical structures shed at the tip of the tabs. An homogeneous Gaussian filter is applied and subtracted from the instantaneous field u to obtain the LES-like decomposed velocity field $u'' = u - \widetilde{u}$. Figure 3.7 illustrates the onset of primary vortical structures in the shear layer and represents a section of the head of hairpin vortices. These hairpin structures appear even in the triangular tabs, where literature suggests their existence only in cases with tabs with non-zero upper width, i.e., in trapezoidal or rectangular geometries [16, 23]. However, the onset of these hairpin structures systematically occurs at larger distances in the triangular tab. These structures are advected downstream with a positive and monotonic inclination in the low *Re*, but exhibit an irregular path and less coherence in the large *Re*. Note that *Re* effects are not restricted to this. As expected, the wake exhibits richer vortex dynamics at the high *Re*. Also, a recirculation zone forming a vortex occurs at the upstream base in all tabs at the low *Re*, while it's absent at the high *Re*. Differences between the tabs on the generation of vortex structures are quantified via the so-called circulation defined as follows:

$$\Gamma = \oint_C \mathbf{v} \cdot d\mathbf{l} = \iint_S (\nabla \times \mathbf{v}) \cdot d\mathbf{S} \tag{3.2}$$

Alternatively, the vortex circulation can be obtained from a tangential velocity profile passing through the vortex core and performing a fit with the Lamb-Oseen vortex model (3.3) [29], which is an exact solution of the N-S equations when cylindrical symmetry is assumed.

$$V(r) = \frac{\Gamma}{2\pi r}[1 - e^{-\frac{r^2}{r_c^2}}] \tag{3.3}$$

By computing the Λ_{ci} in all the samples and determining Γ within a specific range for all the tabs ($x/h_h \in [4, 6]$), we can quantitatively determine the effect of the tab geometry (and geometrical singularities) on the head of the hairpin vortices. A sample of the fitting with the Lamb-Oseen model and variability of the averaged Γ is illustrated in figure 3.8. Table 3.1 summarizes the average circulation and radius of the hairpin vortex core for all tabs and *Re*. These variables are normalized with outer variables (U_o and h_T), and that with the rectangular tab (Γ_r) to highlight the differences between tab geometries. It is noted that the triangular tab induces the weakest vortices and the rectangular tabs the strongest ones. This contrast might suggest that the geometrical singularity is not the leading geometrical property modulating the vortex strength, but the frontal area.

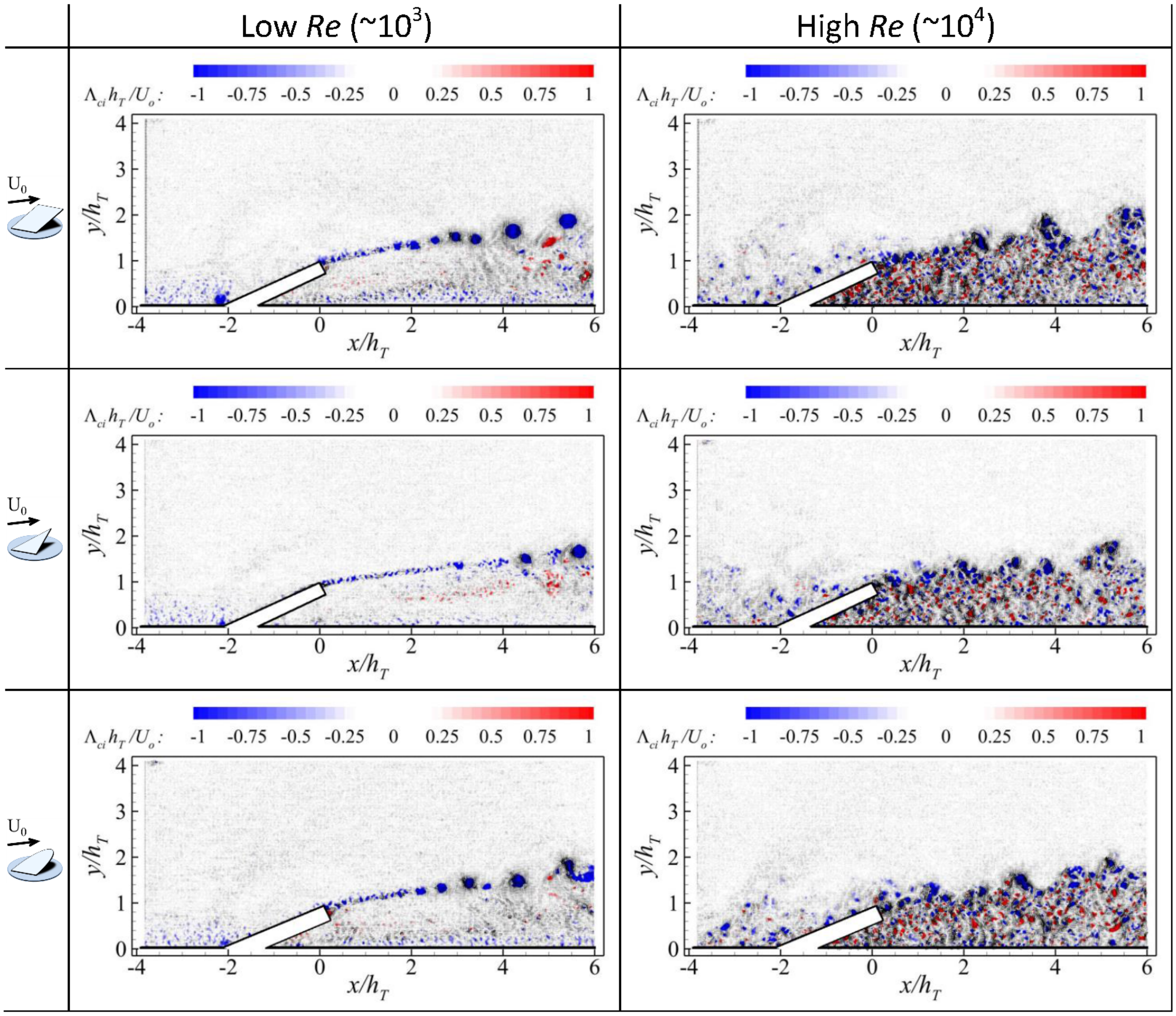

Figure 3.7: 2D contours of Λ_{ci} superimposed LES-like instantaneous filtered vector field around the rectangular, triangular, and elliptical tabs at low Re =2000 and high Re=12900. All the figures share the same color levels to aid comparison.

	Rectangular	Triangular	Ellipsoidal
Γ/U_0h_T	0.53	0.29	0.38
Γ/Γ_r	1	0.55	0.72
r_c/h_T	0.16	0.12	0.13
r_c/r_{cr}	1	0.75	0.81

Table 3.1: Average circulation and vortex core radius of the head of the hairpin vortices.

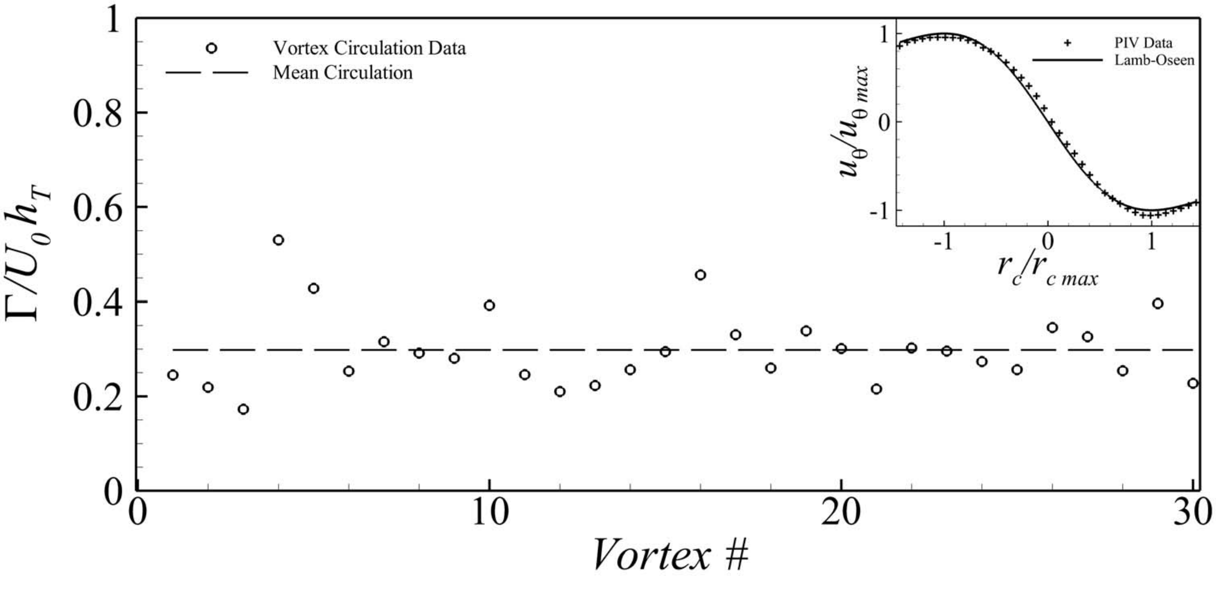

Figure 3.8: Hairpin vortices computed circulation Γ within $x/h_h \in [4, 6]$. Upper-right corner plot shows a sample of Lamb-Oseen curve fitting for a hairpin vortex.

Chapter 4

Conclusions

The tabs geometry affects the coherence of primary vortical structures, with larger impact at lower Re. Higher turbulence in the large Re induces more similar streamwise velocity distribution across the tab due to enhanced mixing. Among the three geometries, the rectangular tab shows to be more efficient enhancing vertical transport. Enhanced turbulent kinetic energy and TKE Production occurs in the shear layer with local maxima around $x/h_T \sim 2-3$ downstream the tab at low Re, while it occurs right past the tab at high Re. The onset of hairpin vortices is observed within the shear layer for all the geometries. In particular, the signature of these structures is quantified for the first time. Differences within the tabs were quantified by the means of vortex circulation and core radius considering the Lamb-Oseen vortex model. The rectangular tab produced, on average, almost twice the circulation produced by the triangular tab and nearly 1.4 times the circulation of the ellipsoidal tab. Also, the average vortex core radius of the rectangular tab-induced hairpin vortices is bigger than the one generated by the other tabs.

Appendix A

Additional Results

A.1 Streamwise Velocity

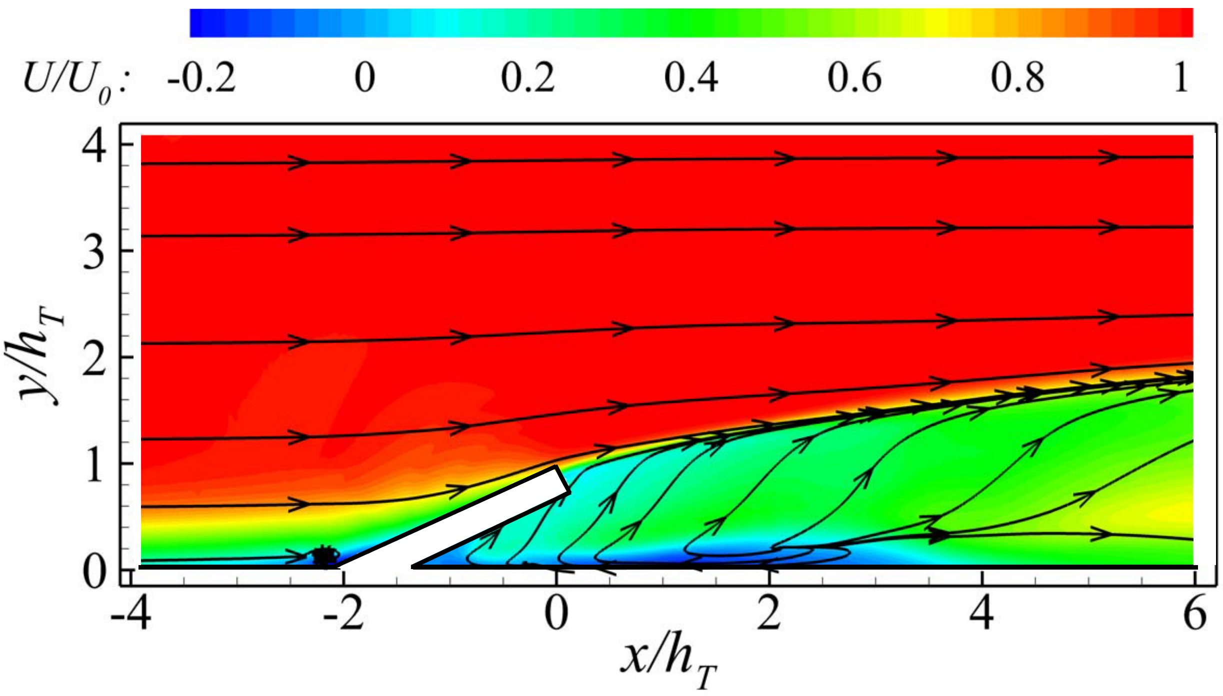

Figure A.1: Normalized streamwise velocity component contour U/U_0 with streamlines. Rectangular tab at low Re.

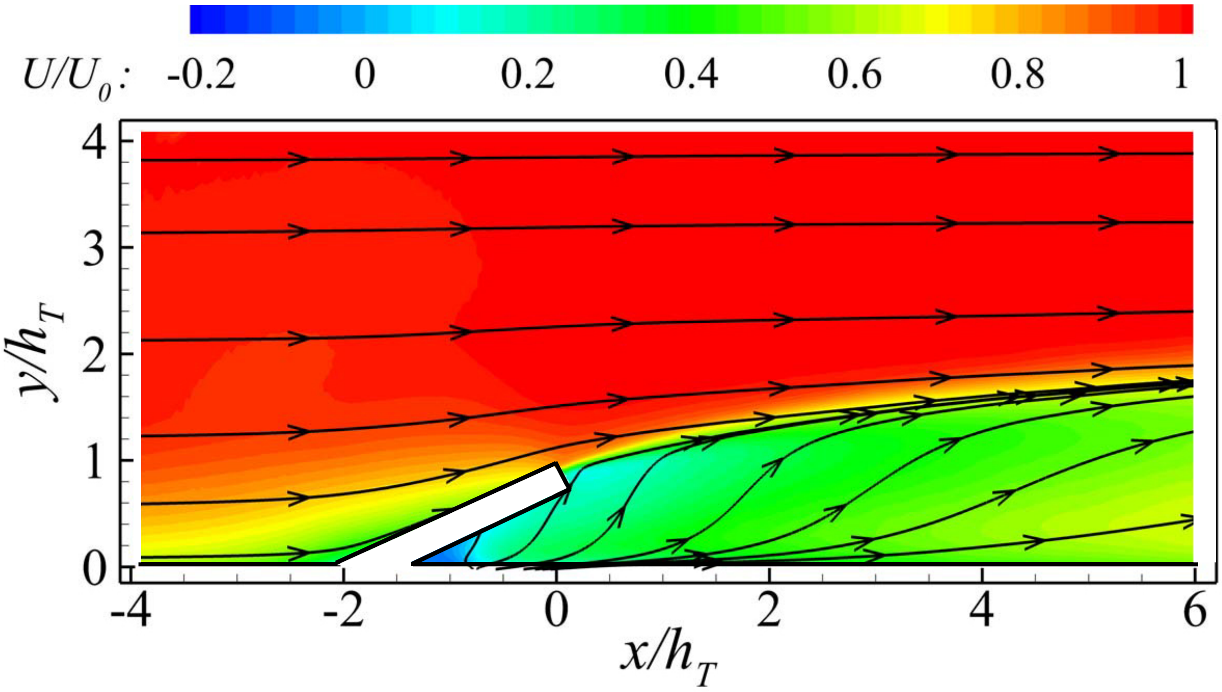

Figure A.2: Normalized streamwise velocity component contour U/U_0 with streamlines. Rectangular tab at high Re.

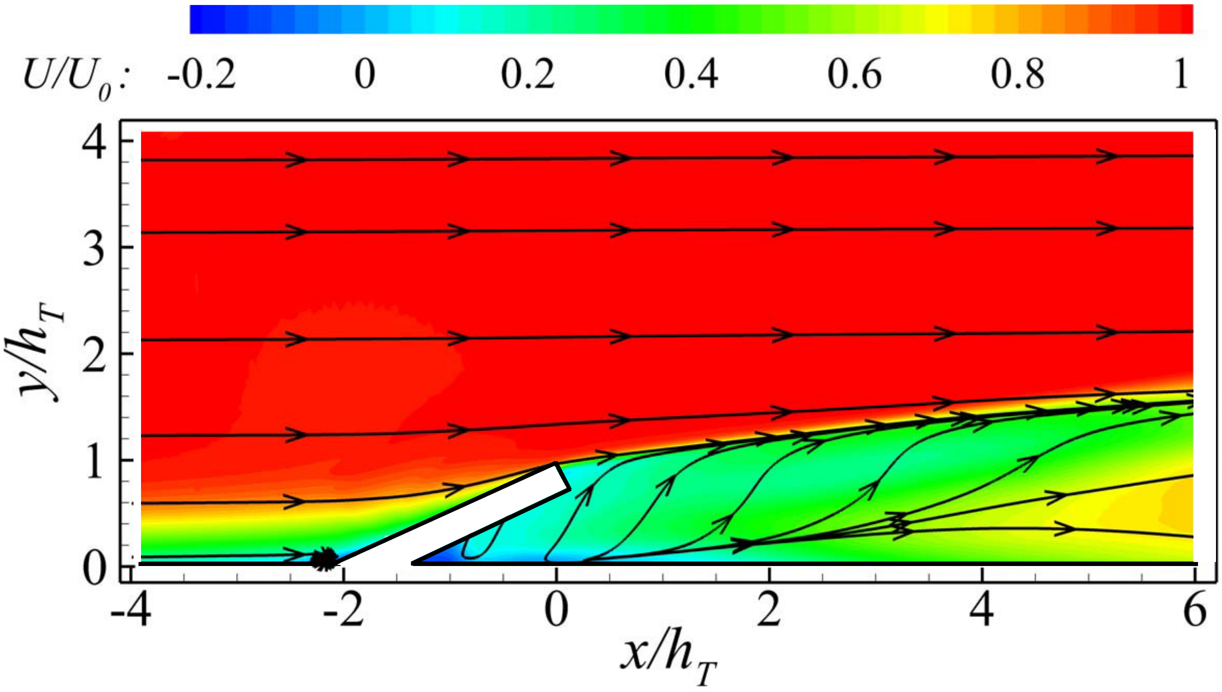

Figure A.3: Normalized streamwise velocity component contour U/U_0 with streamlines. Triangular tab at low Re.

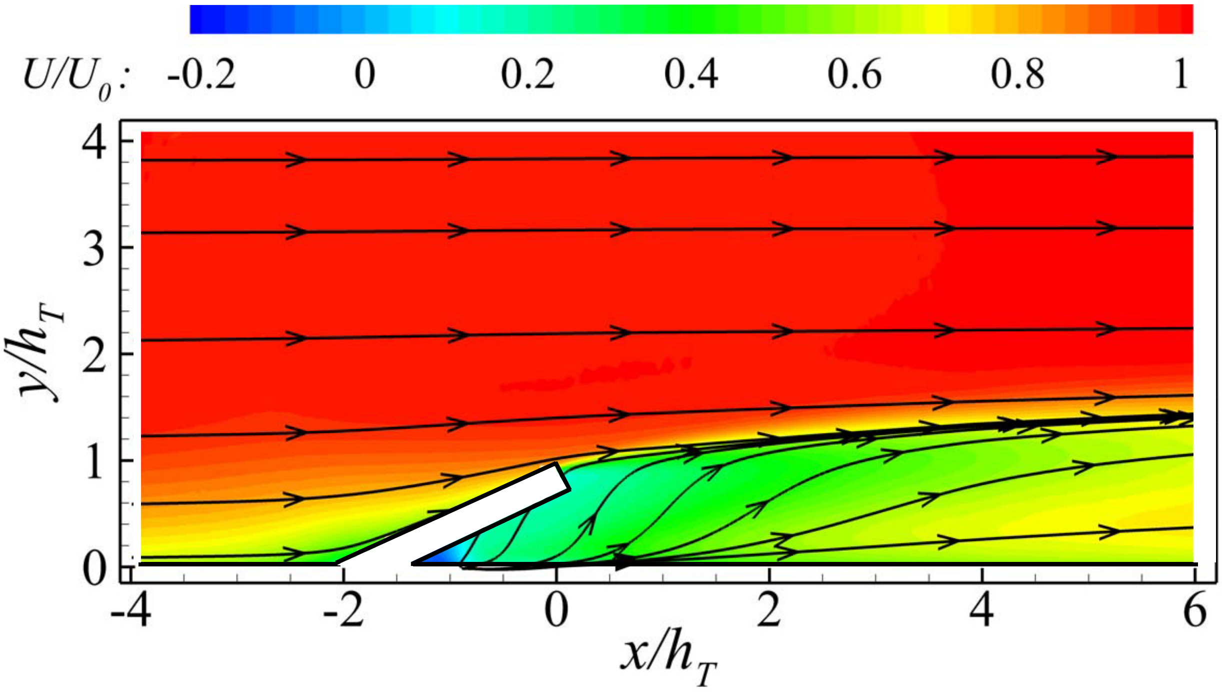

Figure A.4: Normalized streamwise velocity component contour U/U_0 with streamlines. Triangular tab at high Re.

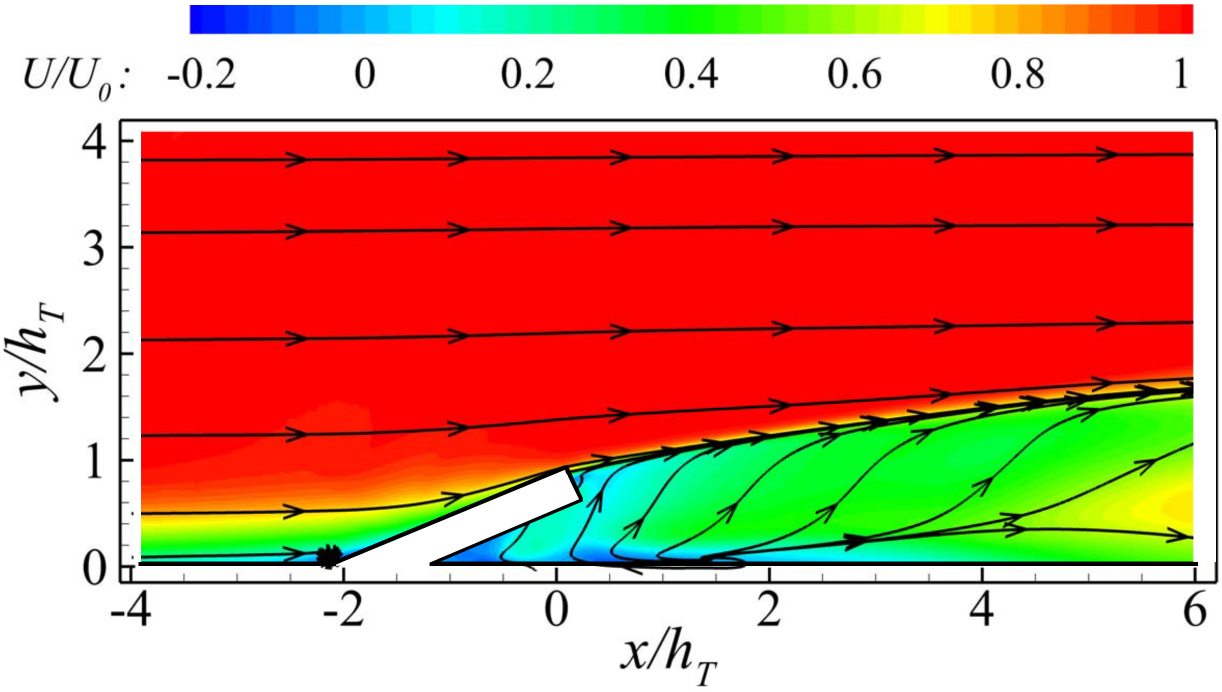

Figure A.5: Normalized streamwise velocity component contour U/U_0 with streamlines. Ellipsoidal tab at low Re

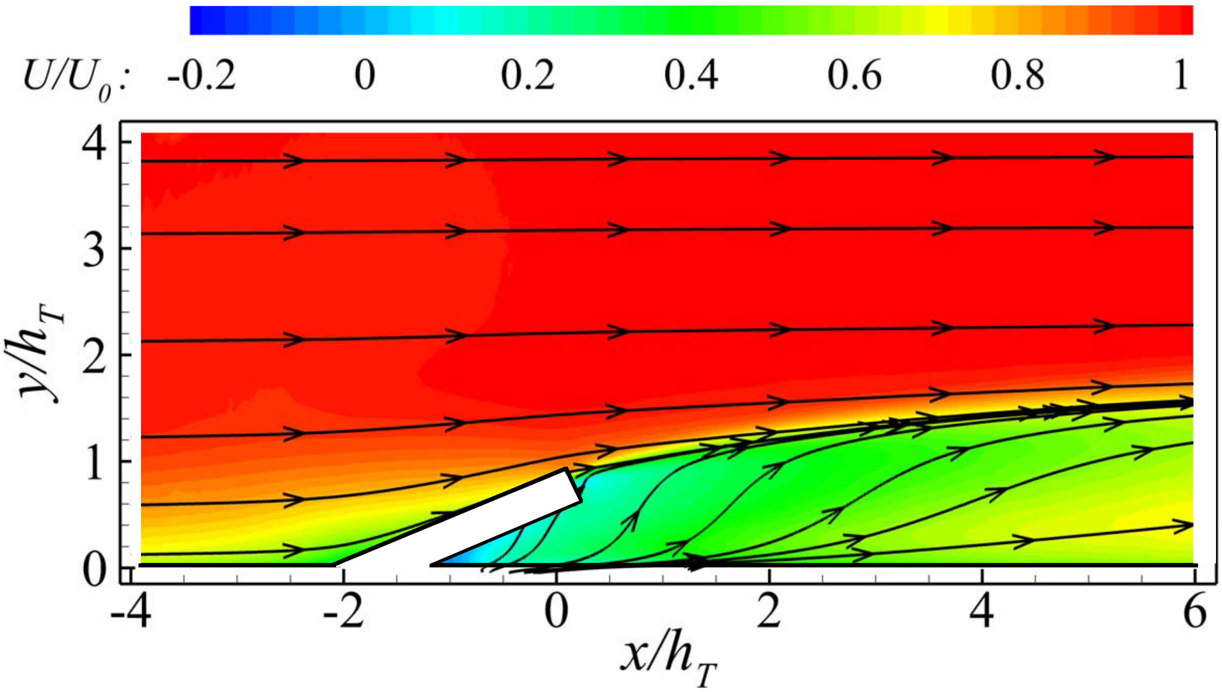

Figure A.6: Normalized streamwise velocity component contour U/U_0 with streamlines. Ellipsoidal tab at high Re

A.2 Instantaneous Vector Fields

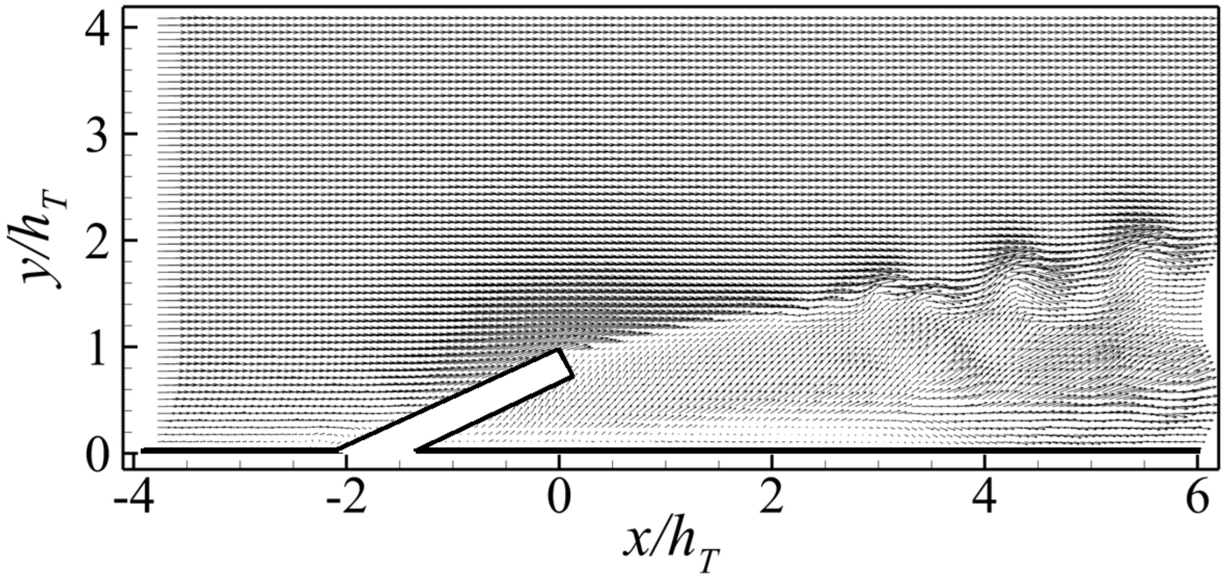

Figure A.7: Instantaneous vector field around the rectangular tab for low *Re*.

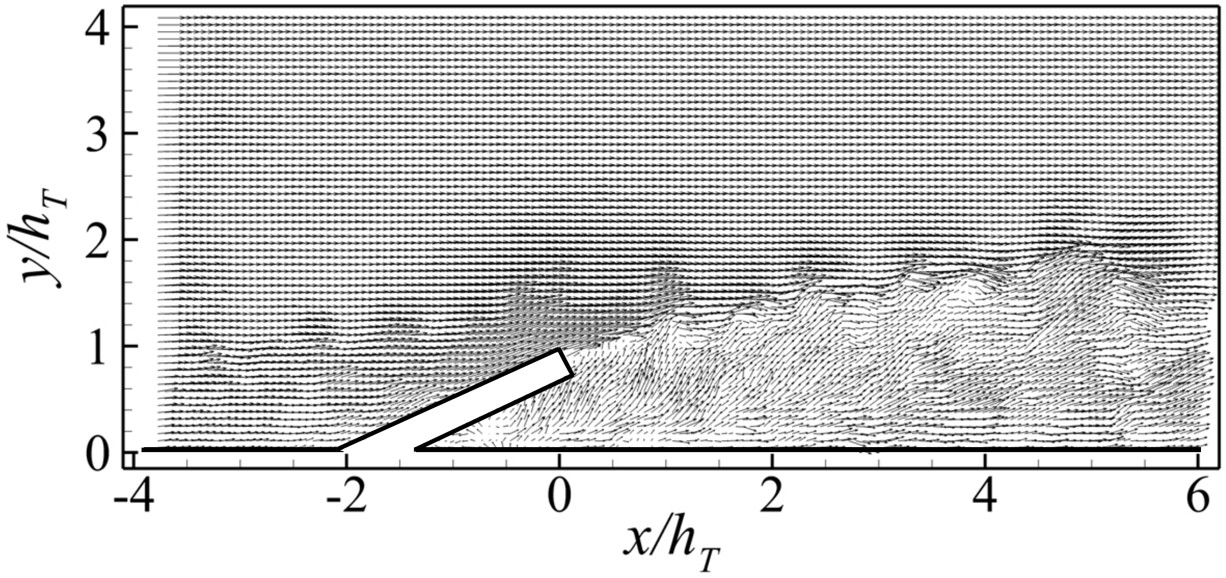

Figure A.8: Instantaneous vector field around the rectangular tab for high *Re*.

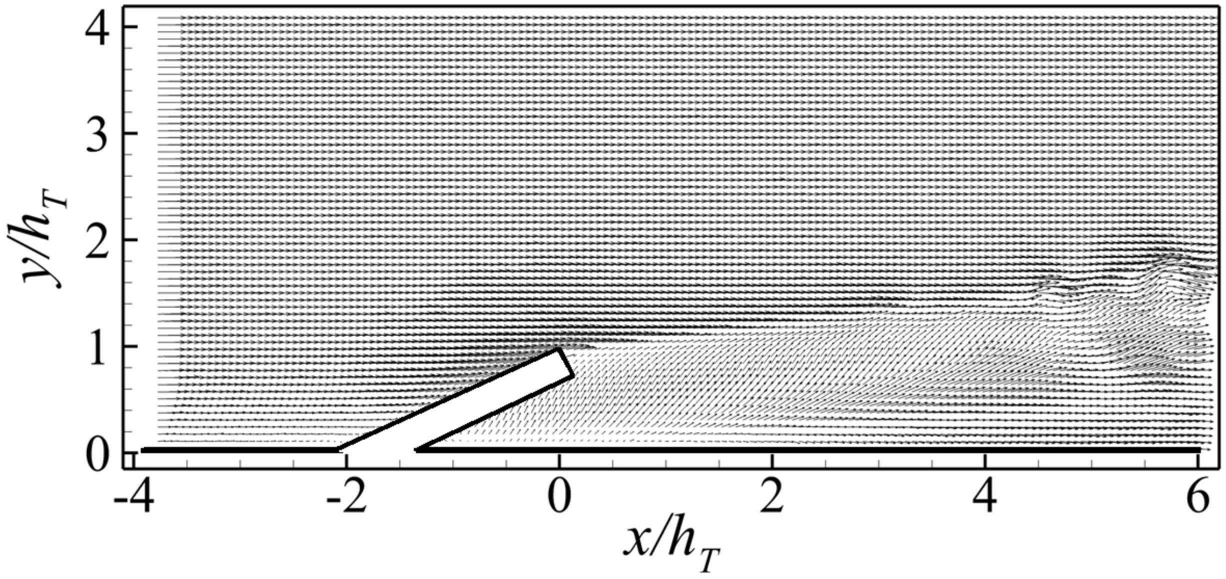

Figure A.9: Instantaneous vector field around the triangular tab for low *Re*.

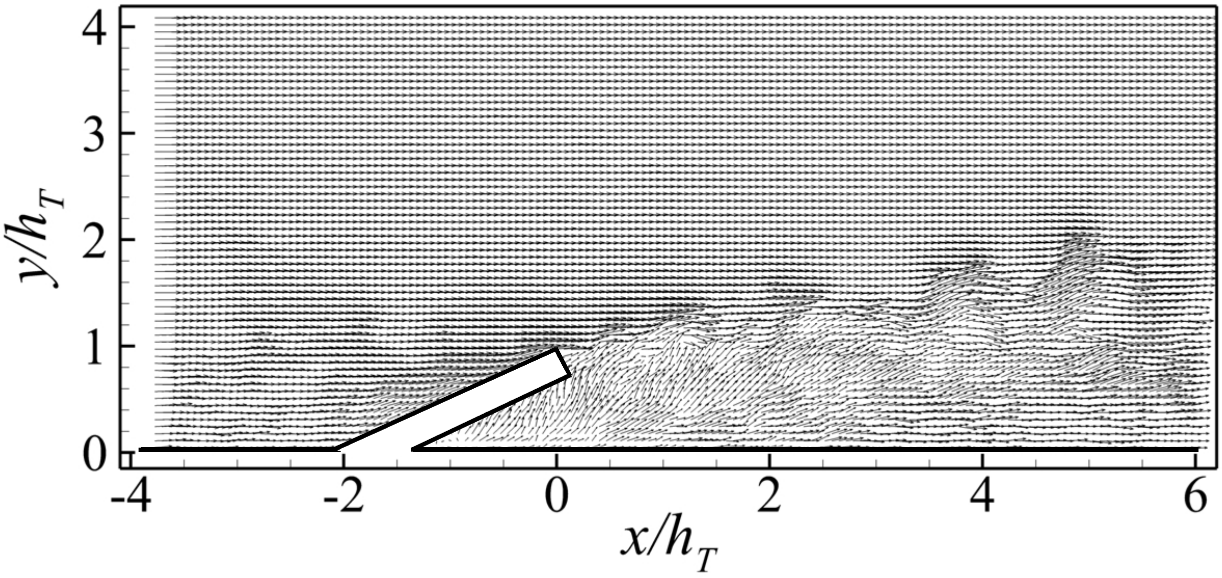

Figure A.10: Instantaneous vector field around the triangular tab for high *Re*.

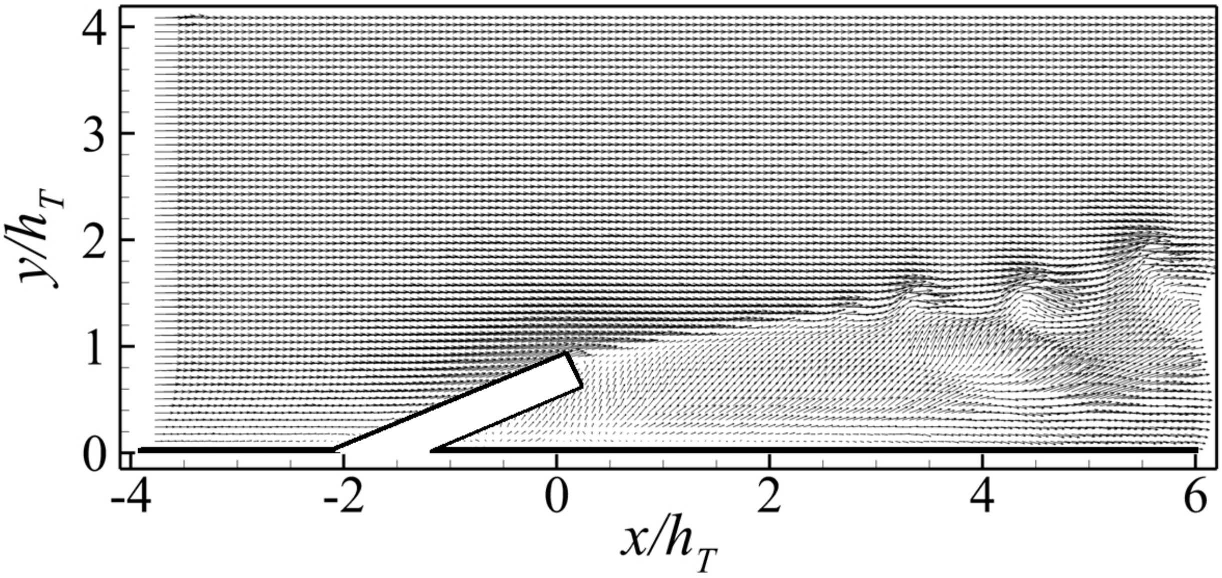

Figure A.11: Instantaneous vector field around the ellipsoidal tab for low *Re*.

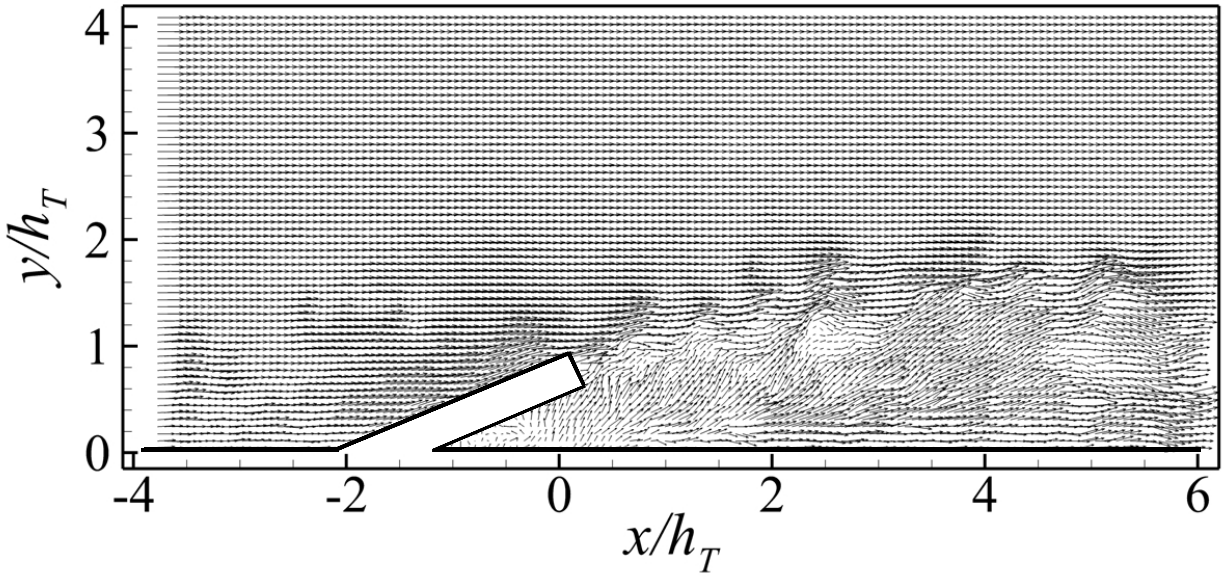

Figure A.12: Instantaneous vector field around the ellipsoidal tab for high *Re*.

A.3 Instantaneous Swirling Strength

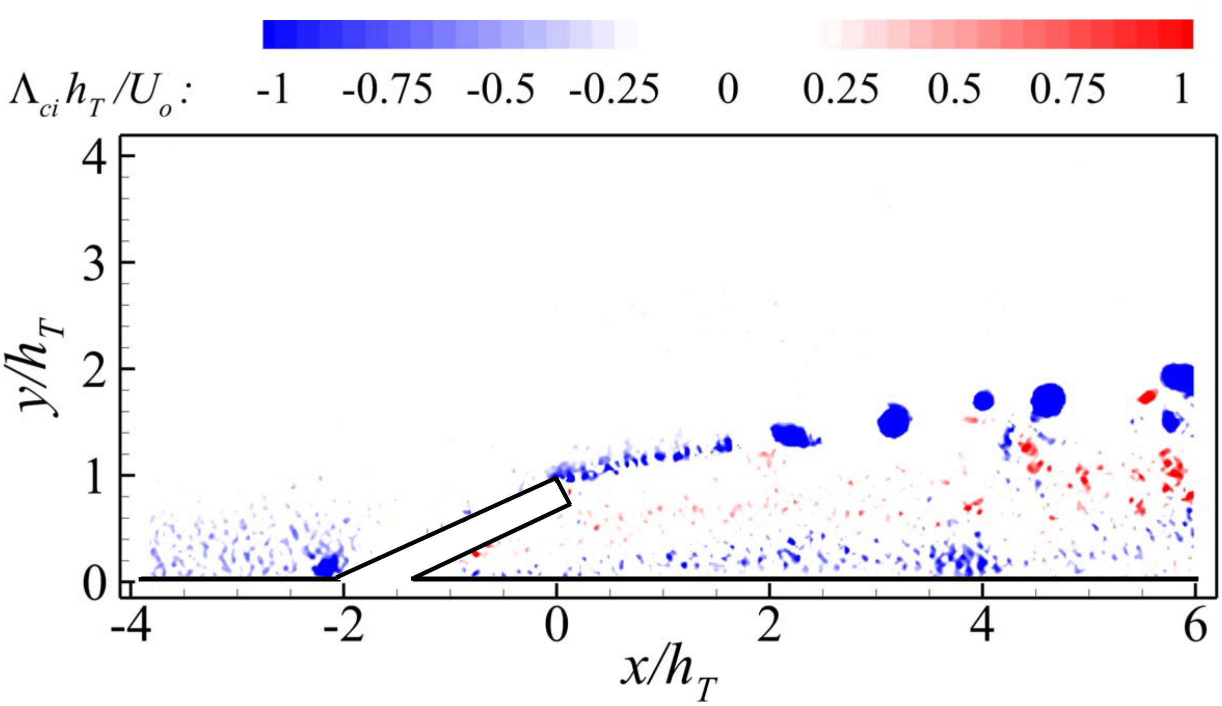

Figure A.13: Instantaneous Λ_{ci} contour around the rectangular tab for low *Re*.

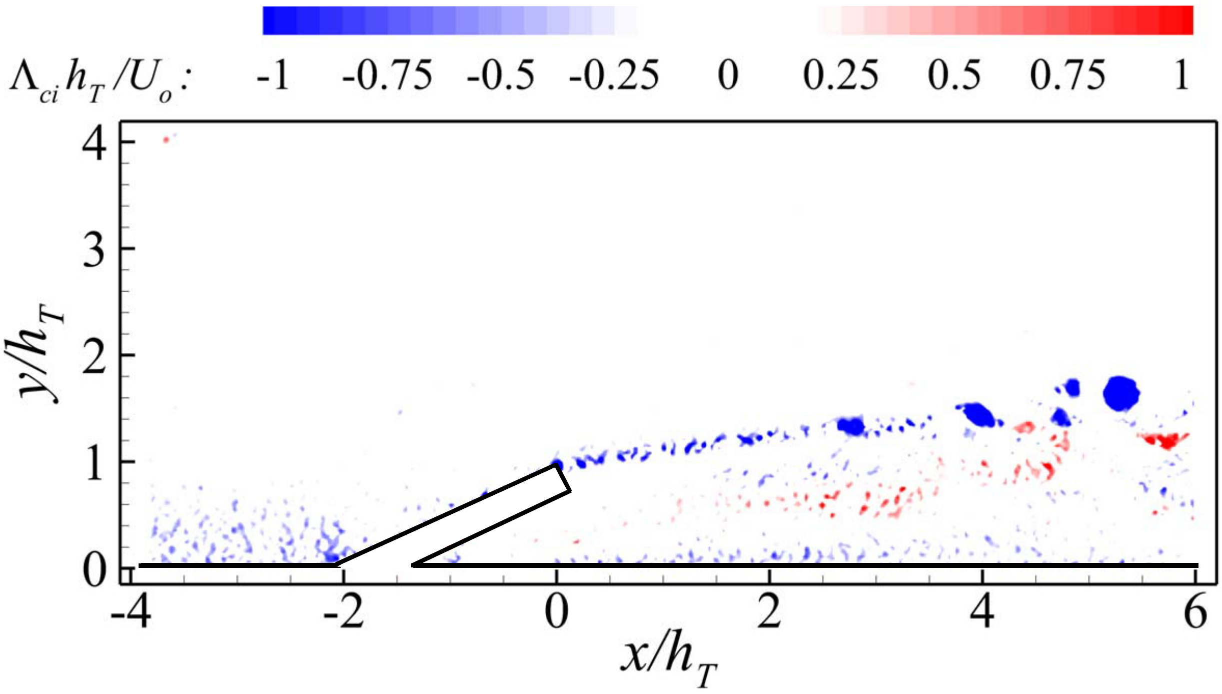

Figure A.14: Instantaneous Λ_{ci} contour around the triangular tab for low *Re*.

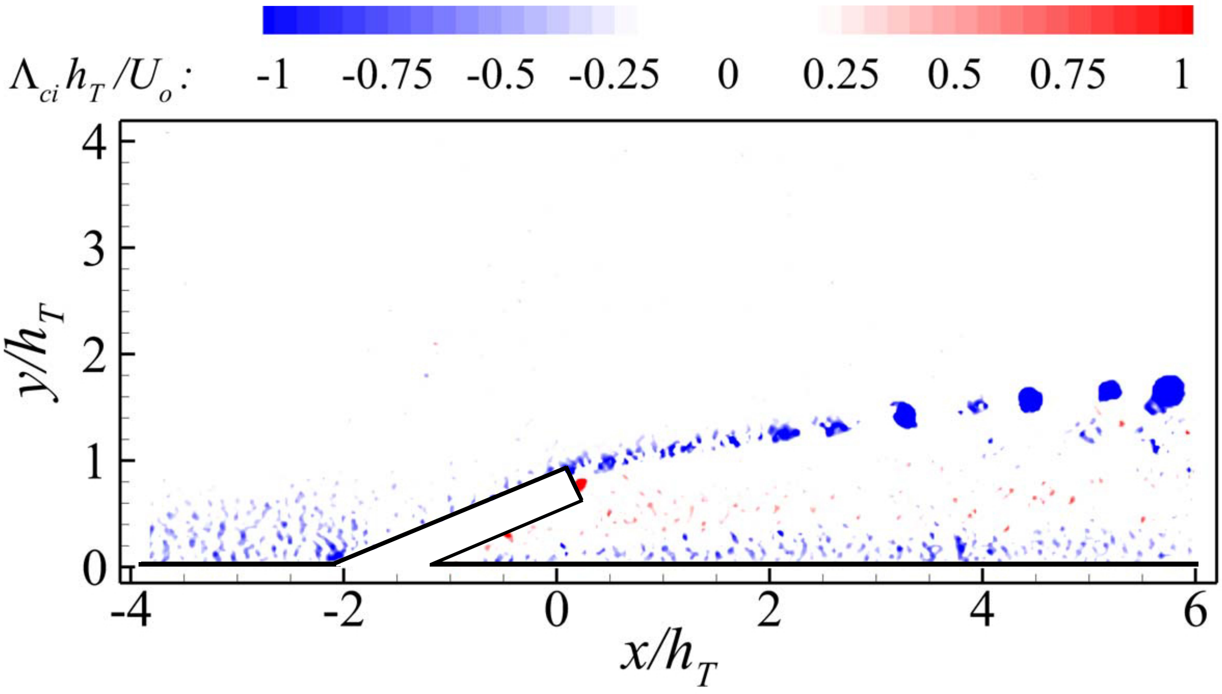

Figure A.15: Instantaneous Λ_{ci} contour around the ellipsoidal tab for low *Re*.

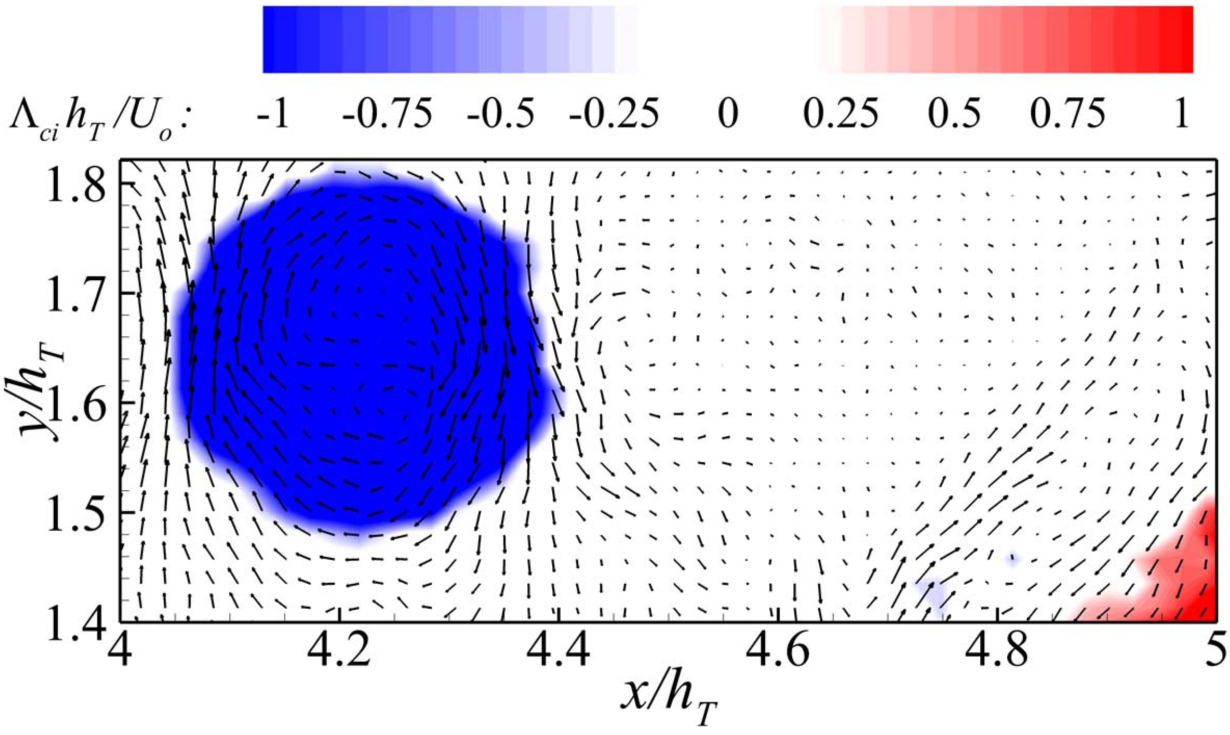

Figure A.16: Λ_{ci} contours and LES-like vector field decomposition near hairpin vortex formation. Rectangular tab at low *Re*.

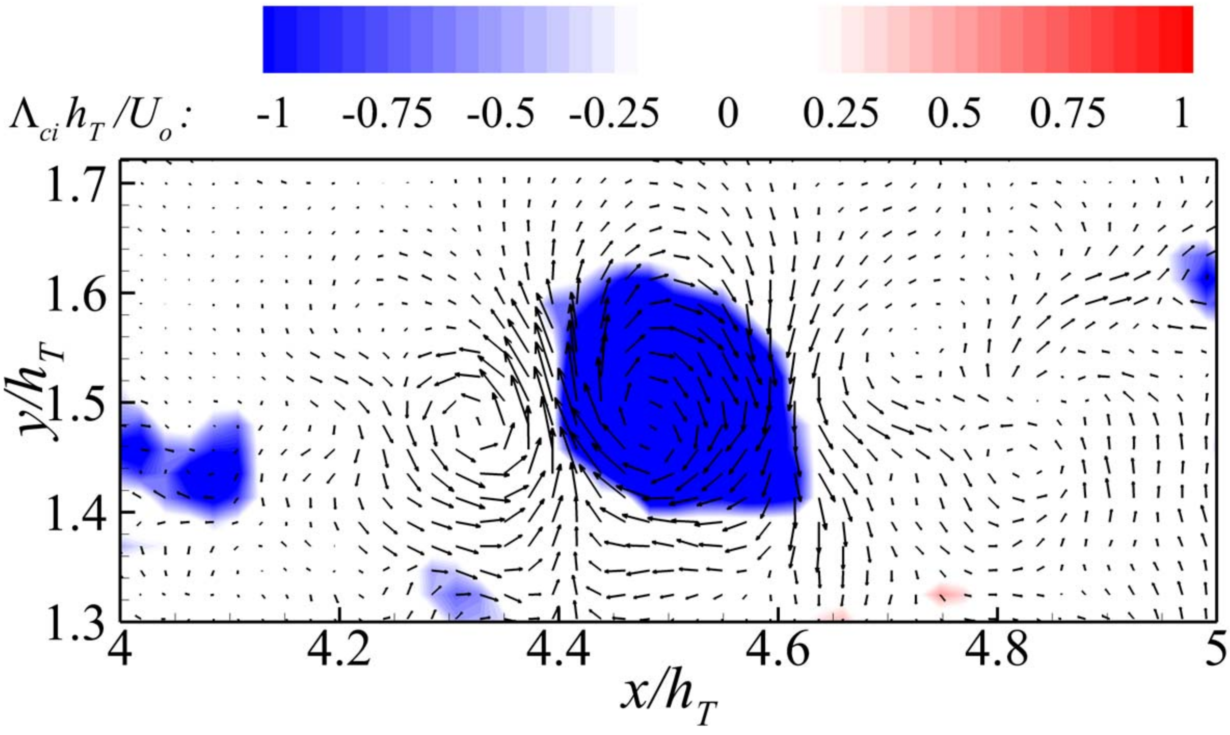

Figure A.17: Λ_{ci} contours and LES-like vector field decomposition near hairpin vortex formation. Triangular tab at low *Re*.

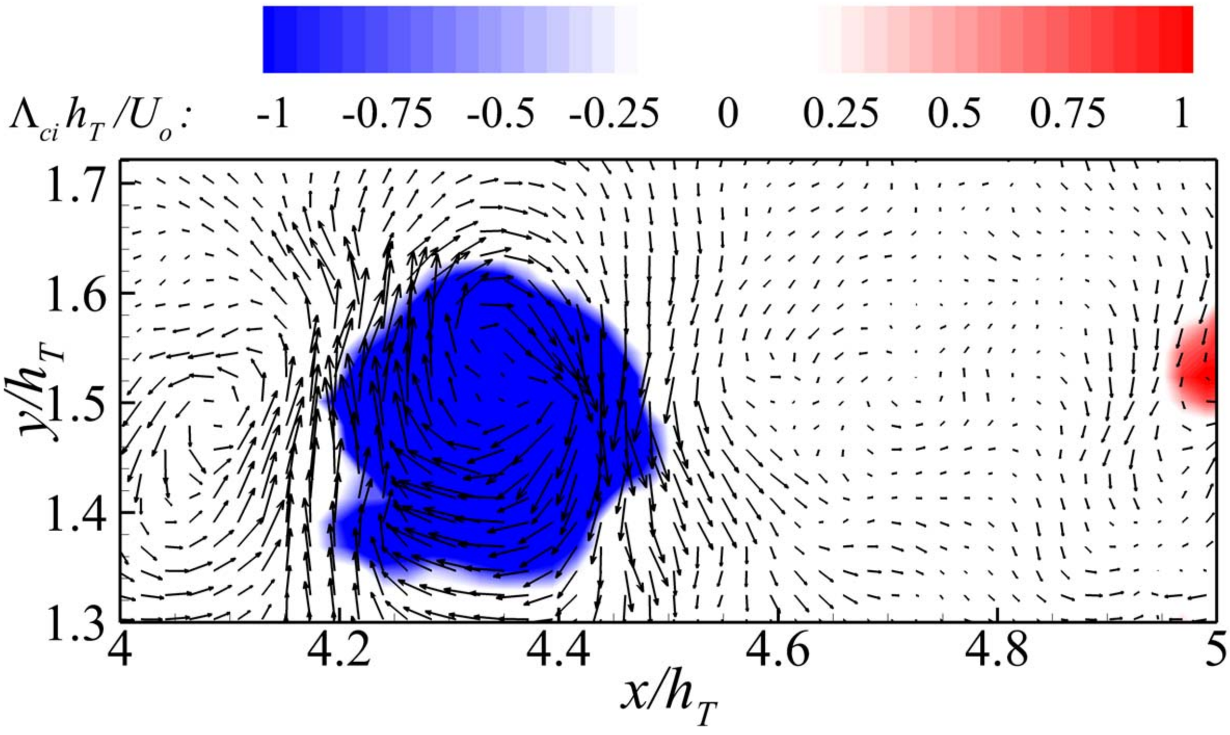

Figure A.18: Λ_{ci} contours and LES-like vector field decomposition near hairpin vortex formation. Ellipsoidal tab at low Re.

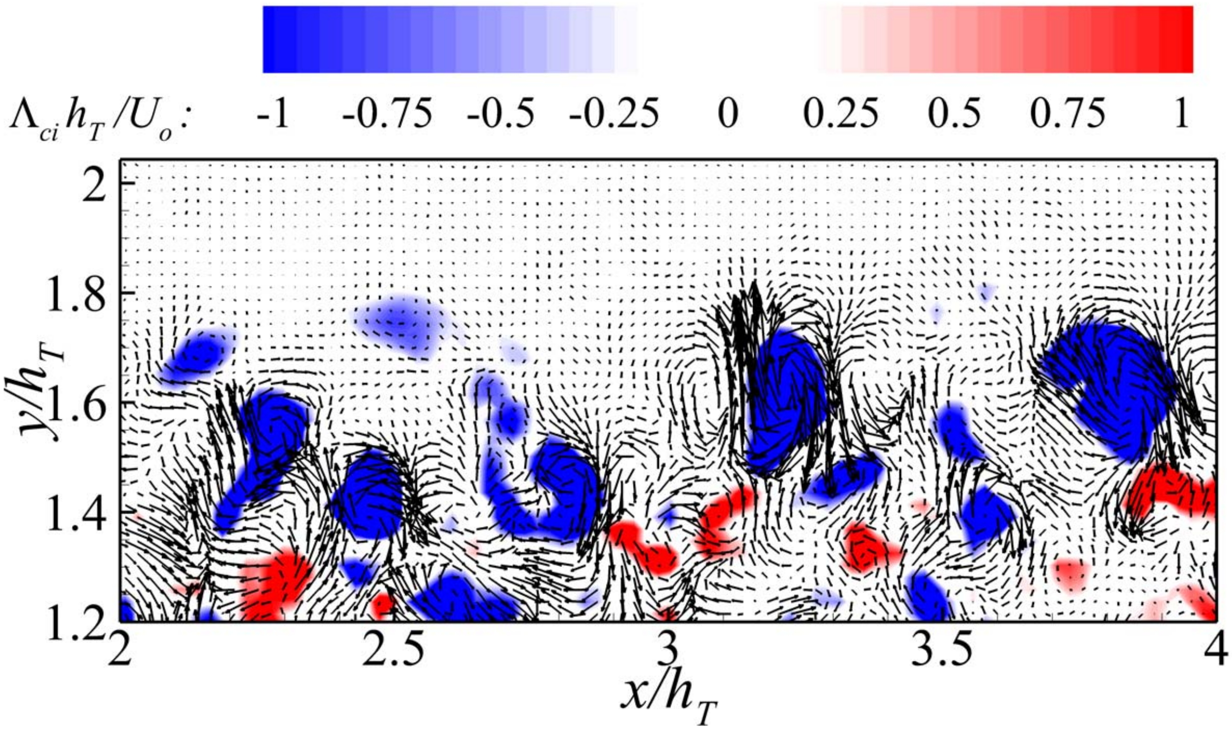

Figure A.19: Λ_{ci} contours and LES-like vector field decomposition near the high shear stress layer. Rectangular tab at high Re.

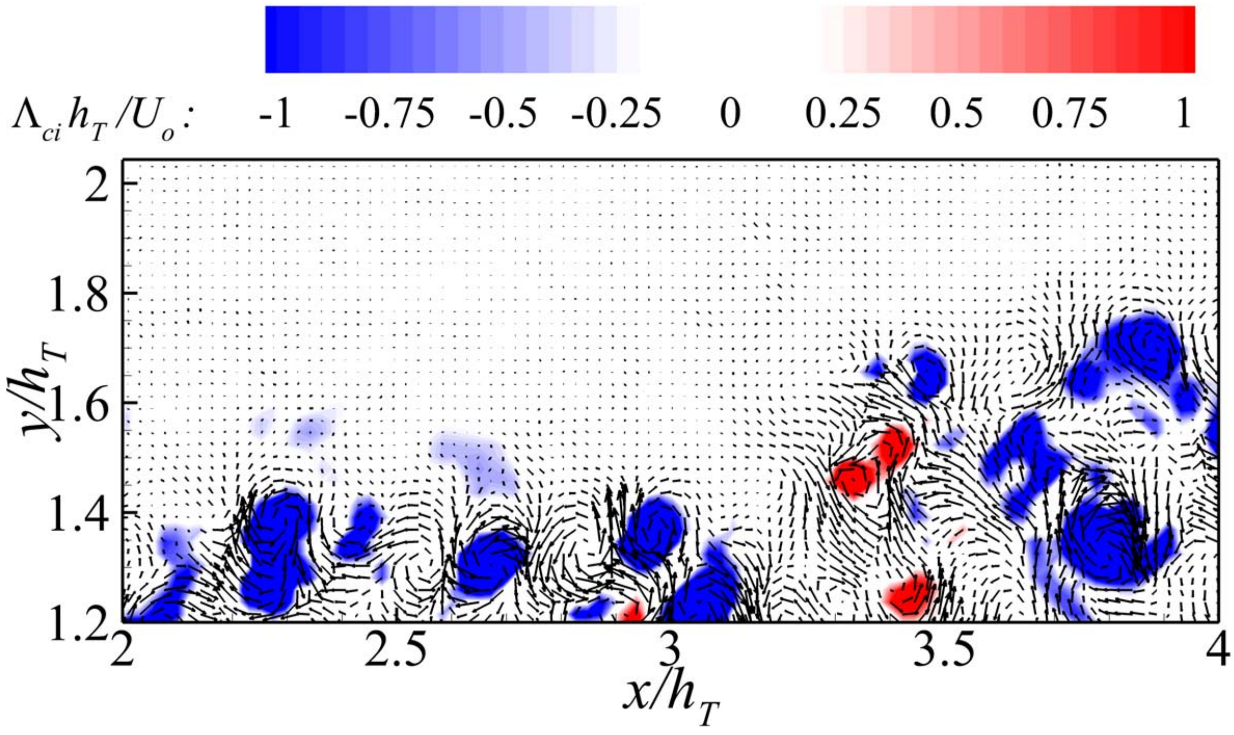

Figure A.20: Λ_{ci} contours and LES-like vector field decomposition near the high shear stress layer. Triangular tab at high Re.

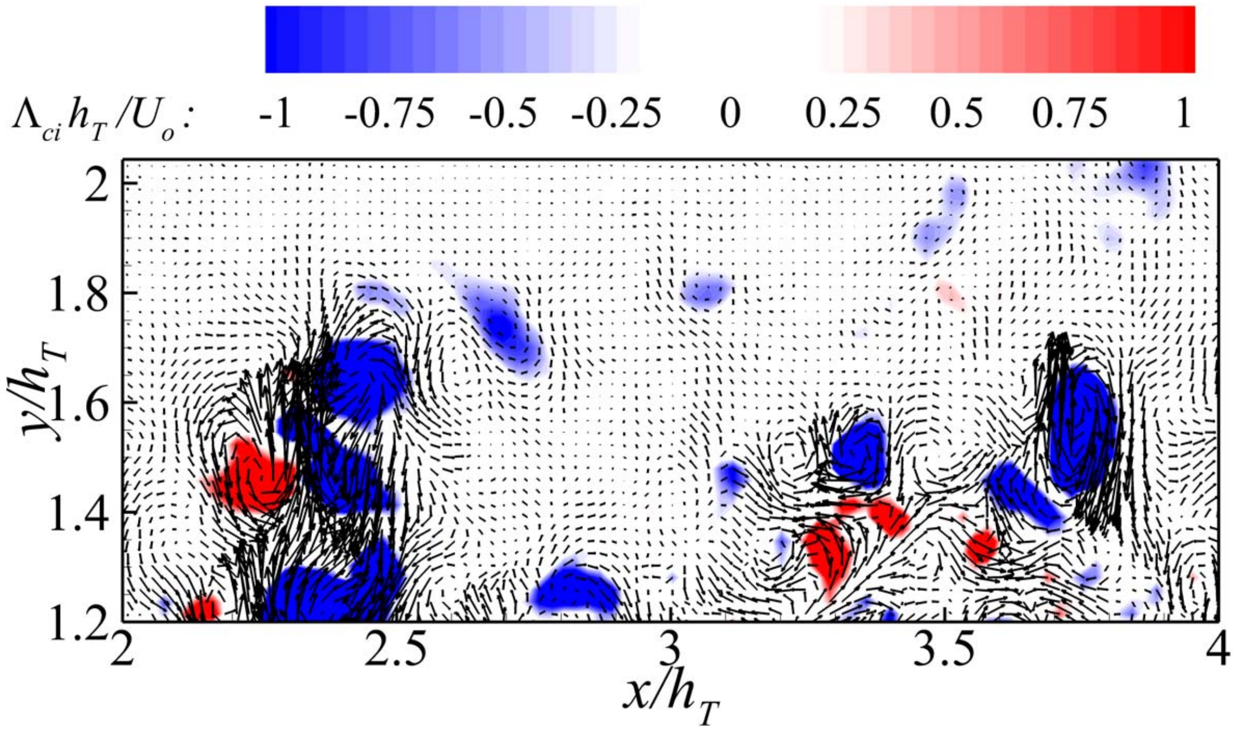

Figure A.21: Λ_{ci} contours and LES-like vector field decomposition near the high shear stress layer. Ellipsoidal tab at high Re.

Appendix B

Specimen Samples and Laboratory Equipment

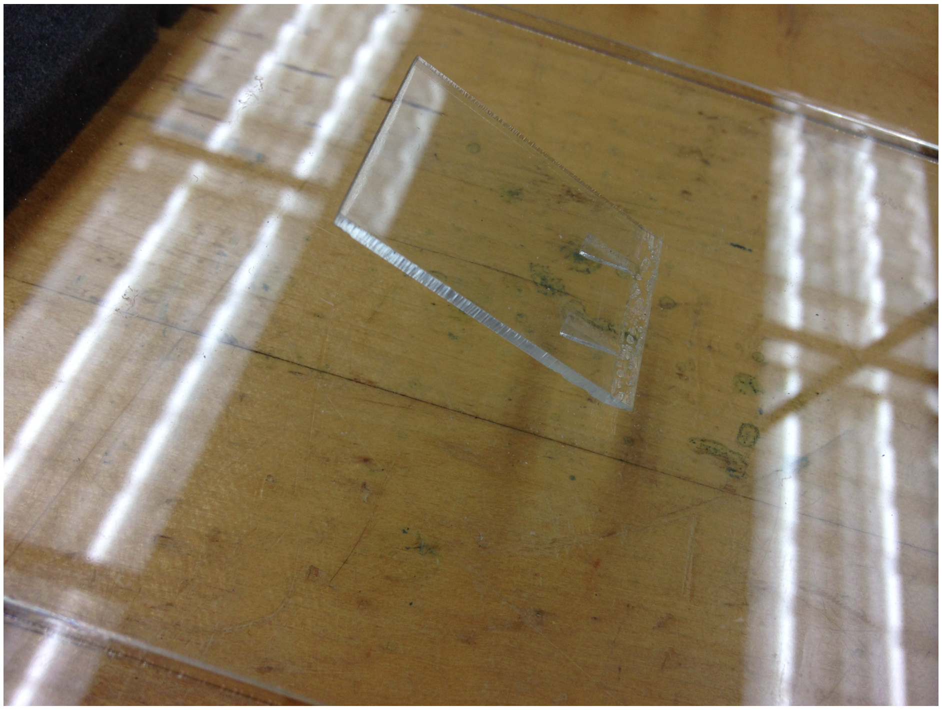

Figure B.1: Fabricated rectangular vortex generator tab used in this research.

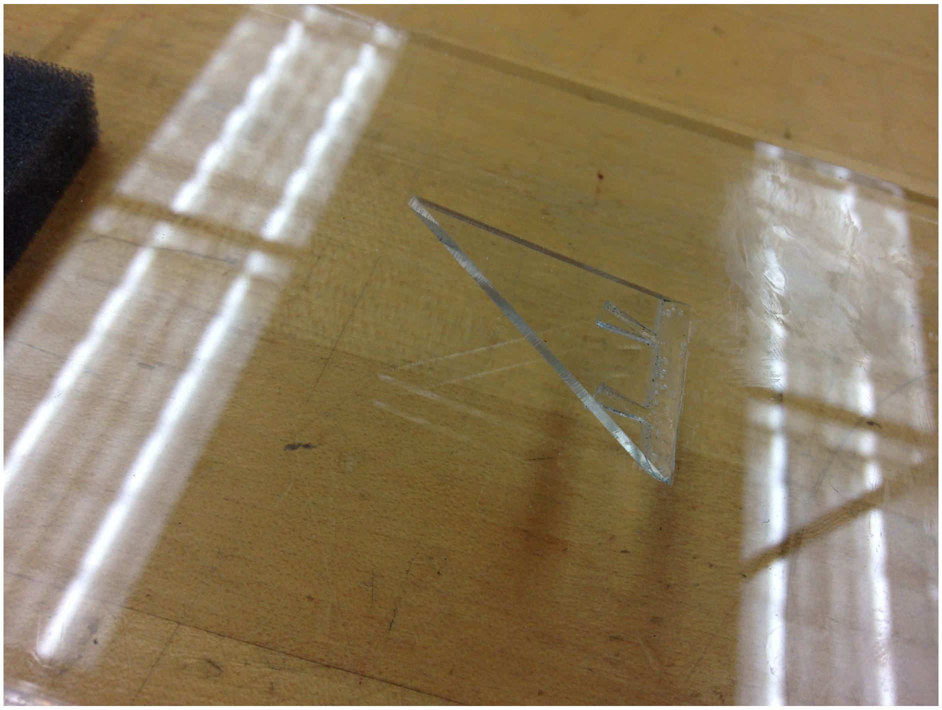

Figure B.2: Fabricated triangular vortex generator tab used in this research.

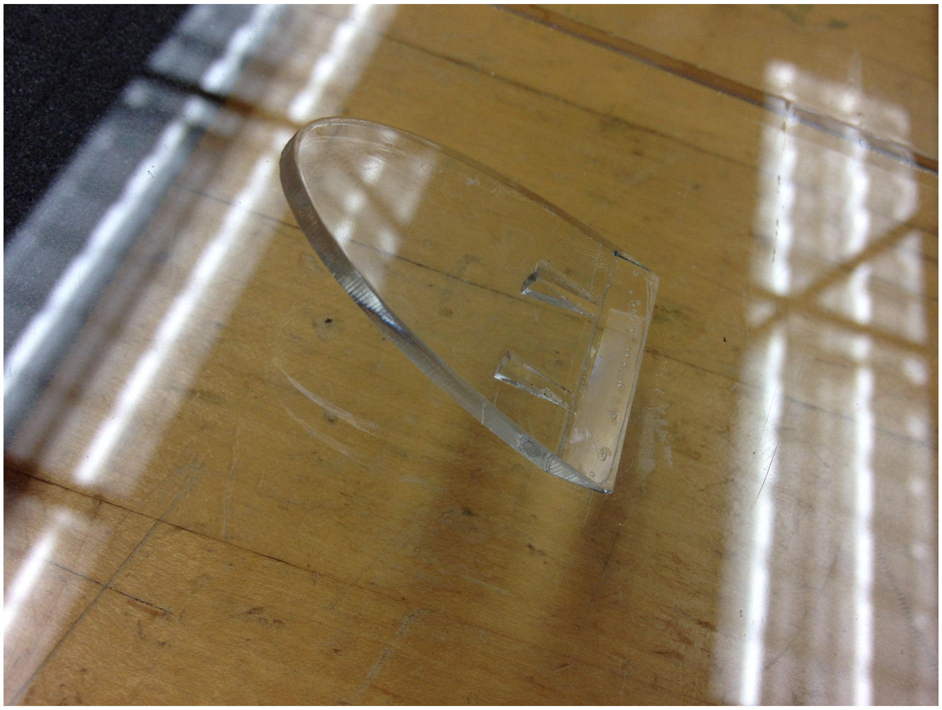

Figure B.3: Fabricated ellipsoidal vortex generator tab used in this research.

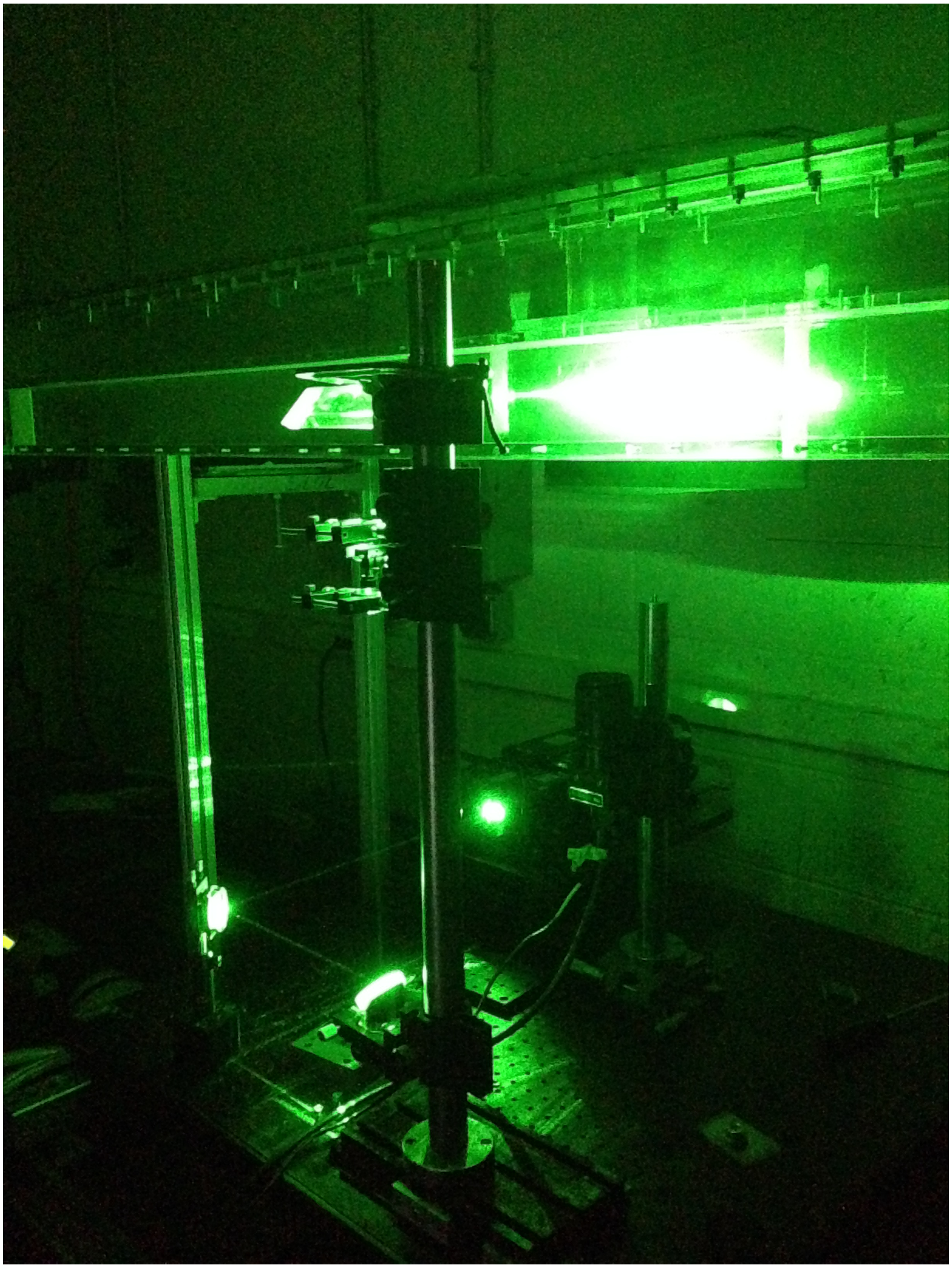

Figure B.4: Laser beam illuminating the test section field of view (FOV).

References

[1] B. Fornberg and A. R. Elcrat, “Some observations regarding steady laminar flows past bluff bodies,” *Philos T Roy Soc A*, vol. 372, no. 2020, 2014.

[2] A. Busciglio, F. Grisafi, F. Scargiali, and A. Brucato, “Mixing dynamics in uncovered unbaffled stirred tanks,” *Chem Eng J*, vol. 254, pp. 210 – 219, 2014.

[3] T.-D. Luong, V.-N. Phan, and N.-T. Nguyen, “High-throughput micromixers based on acoustic streaming induced by surface acoustic wave,” *Microfluid Nanofluid*, vol. 10, no. 3, pp. 619–625, 2011.

[4] H. E. Meijer, M. K. Singh, T. G. Kang, J. M. den Toonder, and P. D. Anderson, “Passive and active mixing in microfluidic devices,” *Macromolecular Symposia*, vol. 279, no. 1, pp. 201–209, 2009.

[5] S.-C. Lin, C.-J. Chang, F.-Y. Wang, H.-C. Hsiao, S.-K. Yang, and C.-Y. Hsiao, “Heat dissipation capacity of heat sink assembly with/without vortex generators,” *Applied Mech Mat*, vol. 598, pp. 288 – 293, 2014.

[6] S. Shi, J.-T. Sun, L.-L. Guo, and G.-S. Du, “Application of vortex generator in ultrasonic heat meter measurement,” vol. 986-987, pp. 1457 – 1460, 2014.

[7] A. Ghanem, C. Habchi, T. Lemenand, D. D. Valle, and H. Peerhossaini, “Energy efficiency in process industry - high-efficiency vortex (hev) multifunctional heat exchanger,” *Renew Energ*, vol. 56, pp. 96–104, 2013.

[8] A. M. Jacobi and R. K. Shah, “Heat transfer surface enhancement through the use of longitudinal vortices: a review of recent progress,” *Exp Therm Fluid Sci*, vol. 11, no. 3, pp. 295–309, 1995.

[9] C.-C. Wang, K.-Y. Chen, and Y.-T. Lin, “Investigation of the semi-dimple vortex generator applicable to fin-and-tube heat exchangers,” *Appl Therm Eng*, 2014.

[10] M. Bragg and G. Gregorek, “Experimental study of airfoil performance with vortex generators,” *J Aircraft*, vol. 24, no. 5, pp. 305–309, 1987.

[11] M. Henze, J. von Wolfersdorf, B. Weigand, C. F. Dietz, and S. O. Neumann, “Flow and heat transfer characteristics behind vortex generators - a benchmark dataset,” *Int J Heat Fluid Fl*, vol. 32, pp. 318–328, FEB 2011.

[12] T.-M. Liou, C.-C. Chen, and T.-W. Tsai, “Heat transfer and fluid flow in a square duct with 12 different shaped vortex generators,” in *Proc. ASME Turbo Expo*, vol. 3, 1999.

[13] H. M. Kaci, C. Habchi, T. Lemenand, D. D. Valle, and H. Peerhossaini, “Flow structure and heat transfer induced by embedded vorticity,” *Int J Heat Mass Tran*, vol. 53, pp. 3575–84, 08 2010.

[14] C. Habchi, S. Russeil, D. Bougeard, J.-L. Harion, T. Lemenand, D. D. Valle, and H. Peerhossaini, “Enhancing heat transfer in vortex generator-type multifunctional heat exchangers,” *Appl Therm Eng*, vol. 38, pp. 14–25, MAY 2012.

[15] L.-H. Tang, S.-C. Tan, P.-Z. Gao, and M. Zeng, “Parameters optimization of fin-and-tube heat exchanger with a novel vortex generator fin by taguchi method,” *Heat Transfer Eng*, vol. 37, no. 3-4, pp. 369 – 381, 2016.

[16] W. J. Gretta, "An experimental study of the fluid mixing effects and flow structure due to a surface mounted passive vortex generating device," Master's thesis, Department of Mechanical Engineering, Lehigh University, Bethlehem, PA, 1990.

[17] W. J. Gretta and C. R. Smith, "Flow structure and statistics of a passive mixing tab," *J Fluid Eng*, vol. 115, no. 2, pp. 255–263, 1993.

[18] O. Lögdberg, J. H. Fransson, and P. H. Alfredsson, "Streamwise evolution of longitudinal vortices in a turbulent boundary layer," *J Fluid Mech*, vol. 623, pp. 27–58, 2009.

[19] C. Habchi, T. Lemenand, D. Della Valle, and H. Peerhossaini, "Turbulent mixing and residence time distribution in novel multifunctional heat exchangers–reactors," *Chem Eng Process*, vol. 49, no. 10, pp. 1066–1075, 2010.

[20] W. Yang, H. Meng, and J. Sheng, "Dynamics of hairpin vortices generated by a mixing tab in a channel flow," *Exp Fluids*, vol. 30, no. 6, pp. 705–722, 2001.

[21] B. K. Hodge and R. P. Taylor, *Analysis and Design of Energy Systems.* Prentice Hall, 3rd ed., 1999.

[22] R. Elavarasan and H. Meng, "Flow visualization study of role of coherent structures in a tab wake," *Fluid Dyn Res*, vol. 27, no. 3, pp. 183–197, 2000.

[23] S. Dong and H. Meng, "Flow past a trapezoidal tab," *J Fluid Mech*, vol. 510, pp. 219–242, 2004.

[24] C. Habchi, T. Lemenand, D. D. Valle, and H. Peerhossaini, "On the correlation between vorticity strength and convective heat transfer," in *In: Proceedings of the IHTC 14, ASME.*, vol. 2, pp. 377–382, 2010.

[25] A. M. Hamed, A. Kamdar, L. Castillo, and L. P. Chamorro, "Turbulent boundary layer over 2d and 3d large-scale wavy walls," *Phys Fluids*, vol. 27, p. 106601, 10 2015.

[26] G. Blois, K. T. Christensen, J. L. Best, G. Elliott, J. Austin, C. Dutton, M. Bragg, M. H. Garcia, and B. W. Fouke, "A versatile refractive-index-matched flow facility for studies of complex flow systems across scientific disciplines," AIAA Inc, 2012.

[27] J. Zhou, R. J. Adrian, S. Balachandar, and T. Kendall, "Mechanisms for generating coherent packets of hairpin vortices in channel flow," *J Fluid Mech*, vol. 387, pp. 353–396, 1999.

[28] A. M. Hamed, Y. Jin, and L. P. Chamorro, "On the transient dynamics of the wake and trajectory of free falling cones with various apex angles," *Exp Fluids*, vol. 56, no. 11, pp. 1–10, 2015.

[29] M. Roth and R. Peikert, "A higher-order method for finding vortex core lines," pp. 143–50, IEEE, 1998.